

Systematic Regional Aerosol Perturbations (SyRAP) in Asia using the intermediate-resolution global climate model FORTE2

Camilla Weum Stjern¹, Manoj Joshi², Laura J. Wilcox³, Ameer Gollop², and Bjørn Hallvard Samset⁴

¹CICERO Center for International Climate Research

²University of East Anglia

³University of Reading

⁴CICERO Center for International Climate and Environmental Research - Oslo

January 15, 2024

Abstract

Emissions of anthropogenic aerosols are rapidly changing, in amounts, composition and geographical distribution. In East and South Asia in particular, strong aerosol trends combined with high population densities imply high potential vulnerability to climate change. Improved knowledge of how near-term climate and weather influences these changes is urgently needed, to allow for better-informed adaptation strategies. To understand and decompose the local and remote climate impacts of regional aerosol emission changes, we perform a set of Systematic Regional Aerosol Perturbations (SyRAP) using the reduced-complexity climate model FORTE 2. Absorbing and scattering aerosols are perturbed separately, over East Asia and South Asia, to assess their distinct influences on climate. In this paper, we first present an updated version of FORTE2, which includes treatment of aerosol-cloud interactions. We then document and validate the local responses over a range of parameters, showing for instance that removing emissions of absorbing aerosols over both East Asia and South Asia is projected to cause a local drying, alongside a range of more widespread effects. We find that SyRAP-FORTE2 is able to reproduce the responses to Asian aerosol changes documented in the literature, and that it can help us decompose regional climate impacts of aerosols from the two regions. Finally, we show how SyRAP-FORTE2 has regionally linear responses in temperature and precipitation and can be used as input to emulators and tunable simple climate models, and as a ready-made tool for projecting the local and remote effects of near-term changes in Asian aerosol emissions.

Hosted file

982020_0_art_file_11683547_s62hqs.docx available at <https://authorea.com/users/713773/articles/698057-systematic-regional-aerosol-perturbations-syrap-in-asia-using-the-intermediate-resolution-global-climate-model-forte2>

Hosted file

982020_0_supp_11682358_s5kn7h.docx available at <https://authorea.com/users/713773/articles/698057-systematic-regional-aerosol-perturbations-syrap-in-asia-using-the-intermediate-resolution-global-climate-model-forte2>

1 Systematic Regional Aerosol Perturbations (SyRAP) in Asia 2 using the intermediate-resolution global climate model 3 FORTE2

4
5 *Camilla W. Stjern¹, Manoj Joshi², Laura J. Wilcox³, Ameer Gollo³, Bjørn H. Samset¹*

6 ¹*CICERO Center for International Climate Research, Oslo, Norway*

7 ²*University of East Anglia, Norwich, England*

8 ³*National Centre for Atmospheric Science, University of Reading, Reading, England*

11 **Abstract**

12 Emissions of anthropogenic aerosols are rapidly changing, in amounts, composition and
13 geographical distribution. In East and South Asia in particular, strong aerosol trends
14 combined with high population densities imply high potential vulnerability to climate
15 change. Improved knowledge of how near-term climate and weather influences these
16 changes is urgently needed, to allow for better-informed adaptation strategies. To
17 understand and decompose the local and remote climate impacts of regional aerosol
18 emission changes, we perform a set of Systematic Regional Aerosol Perturbations (SyRAP)
19 using the reduced-complexity climate model FORTE 2. Absorbing and scattering aerosols are
20 perturbed separately, over East Asia and South Asia, to assess their distinct influences on
21 climate. In this paper, we first present an updated version of FORTE2, which includes
22 treatment of aerosol-cloud interactions. We then document and validate the local responses
23 over a range of parameters, showing for instance that removing emissions of absorbing
24 aerosols over both East Asia and South Asia is projected to cause a local drying, alongside a
25 range of more widespread effects. We find that SyRAP-FORTE2 is able to reproduce the
26 responses to Asian aerosol changes documented in the literature, and that it can help us
27 decompose regional climate impacts of aerosols from the two regions. Finally, we show how
28 SyRAP-FORTE2 has regionally linear responses in temperature and precipitation and can be
29 used as input to emulators and tunable simple climate models, and as a ready-made tool for
30 projecting the local and remote effects of near-term changes in Asian aerosol emissions.

32 **1. Introduction**

33 Aerosol emissions have a wide range of impacts on the climate both near to and far from
34 emission sources, spanning from local changes in surface solar radiation and warming to
35 large-scale modifications of atmospheric circulation patterns and monsoon precipitation (Li
36 et al., 2022; Persad et al., 2023). Anthropogenic aerosols have been found to have an
37 outsized near-term influence on extreme events in recent climate model studies (Samset et
38 al., 2018b). In some regions, anthropogenic aerosol impacts have even been shown to
39 dominate over climate impacts from increasing greenhouse gas emissions. One such region
40 is South and East Asia, which is highly vulnerable to climate risk due to a high population
41 density, rapid industrial development, and severe water stress (Giorgi and Gao, 2018; Wang
42 et al., 2021). The region currently suffers the globe's highest loading of anthropogenic
43 aerosols (Zhang et al., 2012), which have impacted several aspects of Asian climate. Aerosol
44 emission trends have been a key driver of the weakening East and South Asian Summer
45 monsoon, causing widespread summertime drying (Bollasina et al., 2011; Dong et al., 2019;
46 Liu et al., 2017), but have also been linked to increases in extreme precipitation over
47 northwest China (Guo et al., 2022). A significant increase in extreme heat events over China
48 has been moderated by high local anthropogenic aerosol emissions (Chen et al., 2019),
49 which have also contributed significantly to catastrophic floods in southwest China (Fan et
50 al., 2015).

51 Some Asian regions are projected to have potentially large but highly uncertain trends of
52 aerosol emissions in the future (Samset et al., 2019). The strong links between aerosol
53 emissions and Asian climate indicate that future aerosol emission changes are likely to
54 contribute markedly to climate related risk in many highly populated regions. This poses a
55 great adaptation challenge and underlines the urgent need for improved knowledge about
56 the near-term impacts of changes in aerosol emissions.

57 While observational studies are crucial, a deeper understanding of the processes and
58 mechanisms under different aerosol emission pathways necessitates the use of numerical
59 climate models. Many modelling studies have looked at regional perturbations of specific
60 anthropogenic aerosols with the aim of characterizing the physical response. However, while
61 there are important, consistent findings across these model studies, the use of different
62 experiment designs can make it difficult to understand the causes of differences in the

63 results. For instance, regional perturbations of BC over Asia in the Precipitation Driver
64 Response Model Intercomparison Project (PDRMIP, Myhre et al. (2017)), involving a tenfold
65 increase in year 2000 BC concentrations in nine earth system models (ESMs), were found to
66 enhance the low-level monsoon circulation and precipitation (Xie et al., 2020). Dong et al.
67 (2016) use the atmospheric component of HadGEM2-ES and remove all SO₂ emissions over
68 Asia, finding the presence of SO₂ to cause local cooling and a weakening of the East Asian
69 monsoon. Westervelt et al. (2018) performed simulations where they remove BC or SO₄ in
70 different regions, including China and India, and looked at responses compared to a year
71 2000 control simulation. Their three earth system models all showed a local increase in
72 precipitation from removing SO₄ over China, while the local response to removing BC over
73 India varied between the models. Using IGCM4 – the atmospheric component of FORTE2 –
74 Herbert et al. (2022) simulate removal of BC or SO₄ in China or India compared to present-
75 day concentrations in an otherwise similar setup.

76 While the examples above show some robust findings across studies, it is difficult to assess
77 whether differences originate from experiment design or from inherent differences in how
78 the models respond to the forcing. In addition to the challenge of different experiment
79 designs, model complexity also varies between studies. In complex models, where more
80 processes and connections are at play, identifying the physical mechanisms behind a given
81 aerosol signal is more challenging than in simpler models where there are fewer processes
82 involved. For that reason, reduced complexity models – such as FORTE2 – are a useful tool
83 for understanding the physical responses we see in ESMs. They also have the added benefit
84 of speed of integration, which allows for more and longer simulations at lower cost. It is
85 critical, however, that all main mechanisms of aerosol-climate interactions are represented.
86 This notably includes the aerosol-cloud interactions (ACI), which was recently assessed to
87 make up 2/3 of the total anthropogenic aerosol radiative forcing over the historical era
88 (Forster, 2021), but which is generally not represented in reduced-complexity climate
89 models (e.g., Nicholls et al., 2021; Nicholls et al., 2020) . Including ACI is also important for
90 capturing the pattern as well as the magnitude of the forcing (Zelinka et al., 2023). In the
91 present study, we therefore update our reduced-complexity model to include a basic
92 representation of ACI.

93 Using FORTE2, we perform Systematic Regional Aerosol Perturbations (SyRAP) of two
94 different aerosol types (absorbing and scattering) in two different regions (South and East
95 Asia). The linearity of the simulated climate to the strength of the perturbations can readily
96 be tested and, in situations where it holds, the SyRAP simulations can be summed and
97 combined to provide information on climate responses to combinations of aerosol emissions
98 from different regions.

99 The climate impact of regional aerosol perturbations (e.g., Persad and Caldeira, 2018),
100 perturbations of different aerosol species (e.g., Myhre et al., 2017), and comparisons of
101 purely radiative responses versus aerosol-cloud interactions (e.g., Dong et al., 2019) have all
102 been considered in isolation in earlier work. In the framework of the SyRAP concept, we can
103 analyze the relative importance of each of these elements, as well as how they interact,
104 hopefully providing new insight in the topic of regional aerosol impacts.

105 In the next section we describe the FORTE2 model, the aerosol input data, and how ACI are
106 emulated in the model. Section 3 describes the details of the SyRAP simulation setups. The
107 climatology of FORTE2 is described in Section 4, including an account of its representation of
108 important Pacific circulation patterns. Finally, in Section 5, we present responses in a
109 selection of variables starting with core responses in temperature, precipitation, clouds and
110 dynamics, an account of FORTE2 ACI impacts, regional linearity of the perturbations and
111 dependence on the climate state. Simulations and the general FORTE2 responses are
112 summarized in Section 6.

113

114 **2. An updated version of the FORTE2 model, and its aerosol representation**

115 **2.1 The FORTE2 Model**

116 FORTE 2.0 (FORTE2) is an intermediate-complexity coupled atmosphere–ocean general
117 circulation model (Blaker et al., 2021) consisting of the Intermediate General Circulation
118 Model 4 (Joshi et al., 2015) and the Modular Ocean Model-Array (Webb, 1996). The
119 atmospheric model has a standard T42 resolution and 35 sigma layers, extending up to 0.1
120 hPa, while the ocean model has 15 vertical layers going down to 800m depth. The
121 atmospheric model has been used in the past in studies of aerosols over Asia (Herbert et al
122 2022), and its predecessors have been used to explore climate sensitivity (Forster et al.,

123 2000), the importance of the semi-direct effect of absorbing aerosols (Cook and Highwood,
124 2004), climate impacts of explosive volcanic eruptions (Highwood and Stevenson, 2003), and
125 precipitation responses to geoengineering (Ferraro et al., 2014).

126 **2.2 The CAMS reanalysis as aerosol perturbation input data**

127 The global gridded speciated aerosol optical depth and vertical distributions used in SyRAP
128 are based on the Copernicus Atmosphere Monitoring Service (CAMSRA) reanalysis (Inness,
129 2019; Inness et al., 2019). CAMSRA has an 80km (T255) horizontal resolution and provided
130 data from 2003 to 2021 at the time of writing. CAMSRA uses cycle 42R1 of the IFS, which
131 includes an interactive aerosol scheme (Morcrette et al., 2009). Anthropogenic emissions of
132 black carbon, organic carbon, and sulphur dioxide are taken from the MACCity inventory
133 (Granier et al., 2011) for 2003 to 2010, and Representative Concentration Pathway (RCP) 8.5
134 thereafter (Riahi et al., 2011). Biomass burning emissions are from the Global Fire
135 Assimilation System, version 1.2 (GFASv1.2; (Kaiser et al., 2012)). Dust and sea salt emissions
136 are calculated interactively. The reanalysis assimilates aerosol optical depth at 550nm from
137 the Advanced Along-Track Scanning Radiometer (AATSR; (Popp et al., 2016)), and the
138 Moderate Resolution Imaging Spectroradiometer (MODIS) aboard Terra and Aqua (Levy et
139 al., 2013). CAMSRA has smaller biases relative to independent observations than the
140 Monitoring Atmospheric Composition and Climate (MACC) reanalysis and CAMS interim
141 analysis (Xian et al., 2023). For more details of CAMSRA, including key updates compared to
142 previous reanalyses, and an evaluation of the CAMSRA aerosol product compared to
143 previous reanalyses and the Aerosol Robotic NETwork (AERONET; (Holben et al., 1998)), see
144 Inness et al. (2019a).

145 To produce the SyRAP aerosol perturbations used in the experiments described in Section 3,
146 CAMSRA monthly fields of speciated aerosol optical depth and 3D mass mixing ratios for
147 2003-2021 are interpolated to T42 resolution, to produce monthly climatologies of total
148 anthropogenic (BC, OC and SO₄), absorbing (BC and OC), and scattering aerosol (SO₄) optical
149 depth at each gridpoint. Aerosols are not transported in FORTE2. The aerosols are vertically
150 uniform from the 2nd lowest model layer (σ , or $p/p_{\text{surface}} = 0.88$ or approximately 950 m
151 above the surface) until a pressure level p_{min} . p_{min} is defined, for each gridbox, from CAMSRA
152 as 850 hPa or the first pressure level where the 2003-2021 mean mixing ratio of BC+OC+SO₄

153 falls below $5 \times 10^9 \text{ kg kg}^{-1}$, whichever is smaller. Over topography, an additional p_{\min} threshold
154 is set such that $\sigma_{\min} < 0.75$ and $p_{\min} > 300 \text{ hPa}$. Typical values of p_{\min} are 600hPa over much
155 of South Asia and 700hPa over much of East Asia in May. These profiles are then fed into the
156 FORTE2 radiation scheme.

157 **2.3 New Aerosol-cloud-interactions in FORTE2**

158 Aerosol-cloud interactions such as aerosol impacts on cloud albedo or lifetime, are not
159 included in the original setup of FORTE2. However, we include new functionality for SyRAP,
160 used in some of the SO_4 perturbation simulations (Section 3). Within a specified region, ACI
161 is parameterized when aerosol optical depth $\tau > 0.07$. If any of low-level cloud, mid-level
162 cloud, or shallow convective cloud are present, the effective cloud particle radius in those
163 clouds is changed from $15\mu\text{m}$ to $10\mu\text{m}$. (Dong et al., 2019) The $\tau > 0.07$ threshold ensures
164 that ACI forcing does not occur in each gridbox of the specified region, which would be too
165 unrealistic, and gives an ACI distribution in the tropics similar to that seen in CMIP6 models.

166 A potential caveat in the SyRAP set-up, particularly related to the ACI effect, is the
167 experiment design of a zero-aerosol background. As the susceptibility of clouds to
168 microphysical impacts of aerosols tend to be stronger the cleaner the background (Platnick
169 and Twomey, 1994), this is likely to have some impact on the magnitude of the ACI effects in
170 this study. Note, however, that while this would make the clouds in more complex earth
171 system models including a microphysics scheme extremely susceptible to aerosol
172 perturbations, this is not an issue in the simpler FORTE2, where the magnitude of the ACI
173 effect is designed to be comparable to findings in the literature. Note also that ACI effects
174 are only included in two experiments, as described in the next section. The core experiments
175 in this paper include only aerosol-radiation interactions, which should not be sensitive to the
176 background aerosol level.

177

178 **3. Systematic Regional Aerosol Perturbations (SyRAP) in FORTE2**

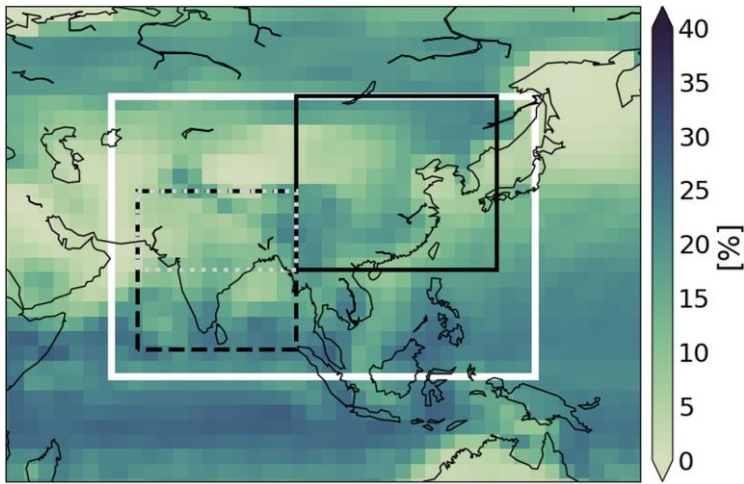
179 **3.1 Core SyRAP simulation overview**

180 In the Systematic Regional Aerosol Perturbation (SyRAP) simulations performed here,
181 baseline simulations with no aerosols are compared to perturbation simulations with added

182 absorbing (black carbon, BC, and organic carbon, OC) or scattering (sulfate, SO₄) aerosols
 183 over India and surrounding regions (“IND”, coordinates 65°E-95°E, 5°N-35°N) or over parts
 184 of East China and surrounding regions (“CHI”, coordinates 95°E-133°E, 20°N-53°N). IND and
 185 CHI are shown as black dashed and solid boxes, respectively, in Figure 1. Aerosols are
 186 perturbed separately in either CHI or IND, or over both regions at once (IND+CHI) – see Table
 187 1 for an overview of the perturbations. The experiments adding BC and OC are labelled “BC”
 188 for simplicity.
 189

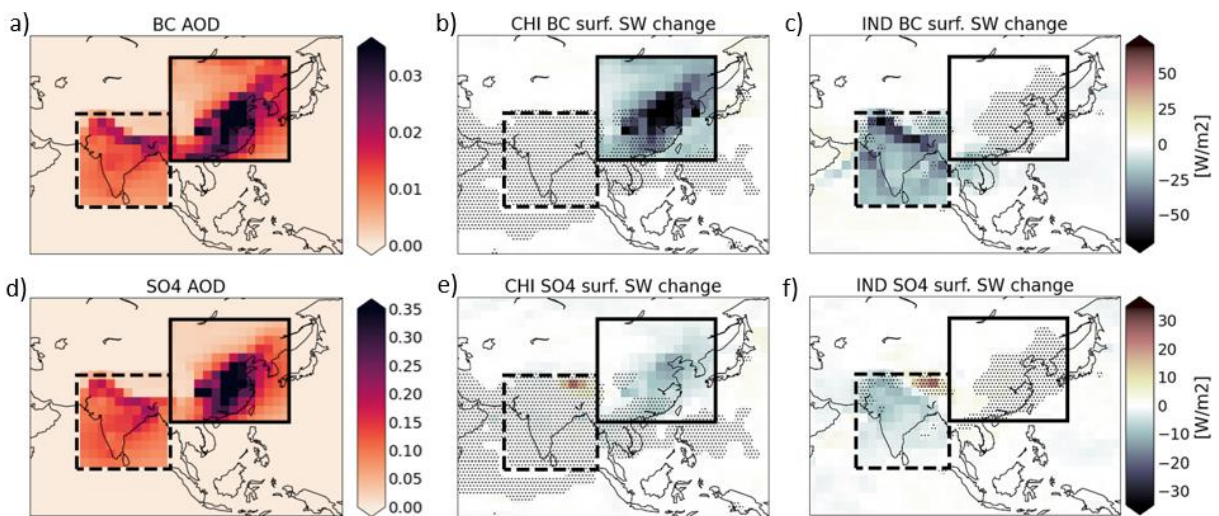
CORE	BC <i>[AOD of added BC+OC]</i>	SO4 <i>[AOD of added SO4]</i>	ACI only	SO4 with ACI	Climate states
IND (India) 65:95E, 5:35N	BC_IND <i>[0.010]</i>	SO4_IND <i>[0.104]</i>	---	---	piC, +1K
CHI (East China) 95:133E, 20:53N	BC_CHI <i>[0.015]</i>	SO4_CHI <i>[0.126]</i>	---	---	piC, +1K
IND+CHI	BC_IND+CHI	SO4_IND+CHI	aci_IND+CHI	SO4aci_IND+CHI <i>Changing effective droplet radius from 15 μm to 10 μm</i>	piC, +1K
LINEARITY TESTS, smaller India region					
NIND (India) 65:95E, 20:35N	BC_NIND	SO4_NIND	---	---	piC
NIND+CHI	BC_NIND+CHI	SO4_NIND+CHI	---	---	piC
ACI SENSITIVITY TEST, done for IND+CHI					
Changing effective droplet radius from 15 μm to 13 μm	---	---	aci_reff13_IND+CHI	SO4aci_reff13_IND+CHI	piC, +1K

190
 191 **Table 1:** SyRAP-FORTE simulations performed for the present study. Each indicated
 192 simulation was run for 200 years. Core simulations are shown in bold, the rest are linearity
 193 or sensitivity tests. “Climate state” refers to the global mean surface temperature change
 194 relative to preindustrial conditions. The geographical regions where aerosol optical depth is
 195 perturbed are shown in Figure 1.



196
 197 **Figure 1:** Map showing the region of applied Aerosol Cloud Interactions in white, as well as the India (IND;
 198 black, dashed), the smaller North India region (NIND; light grey, dotted) and China (CHI; black, solid) regions, on
 199 top of the climatological piC summertime (JJA) convective cloud cover.

200 The added absorbing (BC and OC) and scattering (SO_4) AODs are shown in Figures 2a and d.
 201 The regional mean BC+OC AOD added in the BC_CHI and BC_IND experiments are 0.015 and
 202 0.010, while the regional mean SO_4 AOD added in the SO_4 _CHI and SO_4 _IND experiments
 203 are 0.126 and 0.104. To illustrate the magnitude of these perturbations we show in Fig. 2
 204 the change in surface short wave radiation from adding BC to CHI (panel b) and to IND (panel
 205 c). The panels in Fig. 2e and f show corresponding plots for SO_4 but note that these
 206 perturbations do not include ACI effects of SO_4 . Examples of the impact of the new FORTE2
 207 ACI parameterization will be given in Section 5.2.



208
 209 **Figure 2:** Maps showing the anthropogenic aerosol optical depth (AOD) of a) BC and OC and d) SO_4 within the
 210 China (CHI, solid) and the India (IND, dashed) regions, as well as the response in downwelling surface solar
 211 radiation to adding the BC/OC to b) CHI and c) IND, and the SO_4 to e) CHI and f) IND, respectively. Grey hatching
 212 indicates where responses are not statistically significant.

213 **3.2 ACI implementation**

214 In the SyRAP simulations FORTE2 is for the first time set up with the ability to emulate the
215 indirect aerosol effect – in isolation or in combination with aerosol radiation interactions
216 (ARI). While typically not included in reduced-complexity climate models, aerosol cloud
217 interactions (ACI) account for most of the aerosol forcing globally (Forster, 2021; Zelinka et
218 al., 2014), and there are indications that the ACI is important for the Asian response to
219 aerosol specifically (Dong et al., 2019). The scientific body of evidence points towards
220 dynamical rather than thermodynamical mechanisms dominating the aerosol response over
221 Asia (Tian et al., 2018), making it particularly important to get the total aerosol forcing and
222 its geographical pattern right.

223 The SyRAP ACI simulations allow us to test how important the ACI is for the simulated
224 response to aerosol forcing in this region. The magnitude and pattern of the ACI effect can
225 be easily changed in the model set-up, by scaling the applied effective radius anomaly and
226 scaling the aerosol optical depth at which cloud changes occur, respectively. This flexibility
227 can be used to provide insight into, for instance, why ESMs differ in their responses to
228 standardised aerosol emission changes. The ACI can be turned on even when the direct
229 aerosol radiative forcing is turned off, so that the effects of nonlinearities when including ACI
230 can be assessed.

231 Since the ACI effects of aerosol from China and India are hard to disentangle in reality, and
232 as aerosol is not transported in SyRAP, the ACI runs were only done for the experiments
233 perturbing SO₄ in the combined IND+CHI region. For these experiments, ACI is parametrized
234 within a box bounded by coordinates 60°E-140°E, 0°N-53°N (see white box in Fig. 1). The
235 region where ACI is prescribed is chosen to capture regions where significant ACI-induced
236 changes in cloud properties were seen in response to regional aerosol perturbations in
237 HadGEM3 (Dong et al., 2019). In that model, the ACI was shown to be important for the local
238 precipitation response, partly by changing the response in the season when the forcing
239 occurs, and partly by preconditioning the SST pattern that governs the response in later
240 seasons.

241 As shown in Table 1, we simulate the ACI effect on top of the default radiation-only
242 experiment (SO4aci_IND+CHI), but also the ACI-only effect (aci_IND+CHI). In addition, we do

243 sensitivity tests reducing the magnitude of the ACI by reducing droplet sizes from 15 to 13
244 μm , as opposed to from 15 to 10 μm in the regular ACI runs. These runs will be discussed in
245 Section 5.2.

246 **3.3 Background climate states**

247 The conditions under which aerosols influence climate are not constant in time. For instance,
248 GHG-induced warming may change cloud distributions and properties, influencing the
249 pattern and magnitude of aerosol forcing, or change the monsoon climatology to which
250 aerosol forcing is being applied, potentially introducing nonlinearities. To understand how
251 aerosol impacts depend on global warming level, we perform all aerosol perturbations in
252 different baseline climates: one with preindustrial CO_2 levels (280 ppmv, piC) and one with
253 approximately present-day CO_2 levels for which climate is about 1 degree warmer (500
254 ppmv, +1K). We also did a baseline simulation with future CO_2 levels for which climate is
255 about 2 degrees warmer than preindustrial conditions (850 ppmv, +2K). The relatively large
256 CO_2 concentrations in the latter two runs reflect the low climate sensitivity of IGCM4 of 2.1K
257 on doubling CO_2 (Joshi et al., 2015) and subsequent low transient climate response of
258 FORTE2.

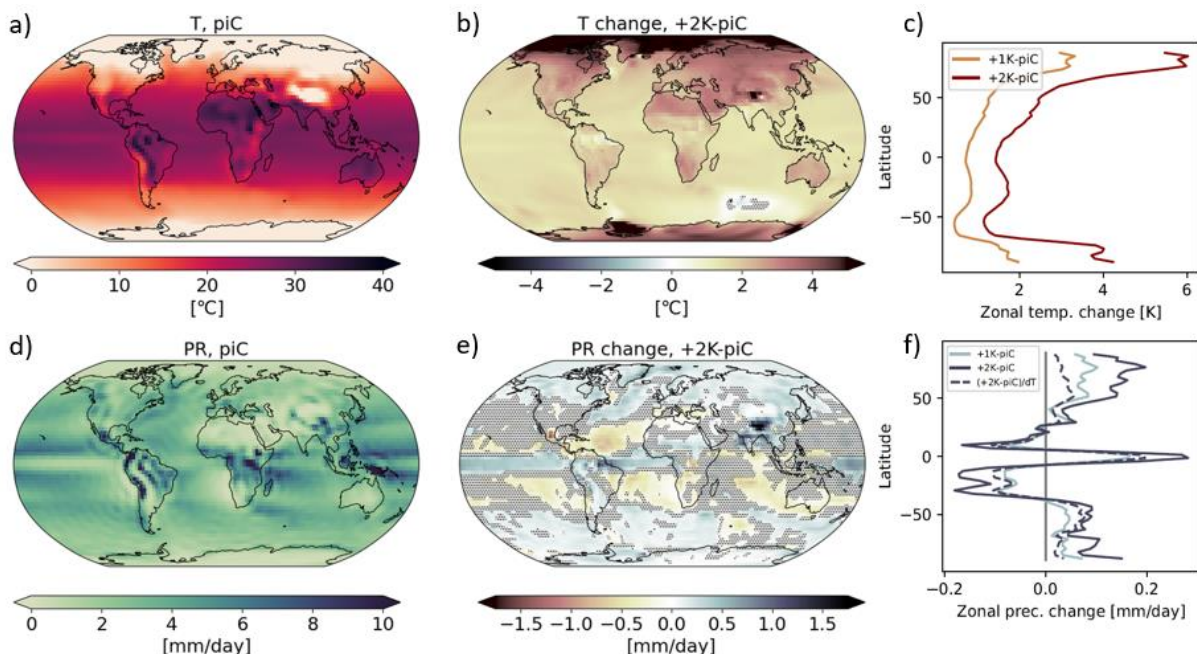
259 In addition to the core experiments, we also perform an additional set of experiments where
260 the IND region is reduced to a much smaller region comprising only the northern parts of
261 India (“NIND”, Table 1). This region is marked in light grey dotted lines in Fig. 1. These
262 simulations will be used when addressing the regional additivity of the climate response to
263 the CHI and IND aerosol perturbations, as discussed further in Section 5.3.

264 All simulations are run for 200 years, enabling studies of radiative responses over a timescale
265 of < 1 year, fast surface ocean responses on timescales of 10-30 years, and slower deeper
266 ocean changes and equilibrium climate responses. All figures in the present analysis show
267 averages for years 51-200, with the first 50 years discarded to let the climate state
268 equilibrate. Climate responses are calculated as the mean response for a perturbation
269 experiment minus the mean response for the corresponding control simulation. For each
270 grid cell, we perform a two-tailed Student’s t-test to identify where differences between the
271 control and perturbed simulation are statistically significant at the 5% level. In map plots, we
272 add hatching to areas where changes are *not* statistically significant.

273 4. FORTE2 climatological characteristics

274 4.1 Baseline climatology

275 The climatological distribution of temperature and precipitation in the baseline (piC)
276 simulations are shown in Fig. 3 a) and d), respectively. A thorough evaluation of the
277 preindustrial climatology of FORTE2 was conducted in Blaker et al. (2021). Blaker et al.
278 (2021) show that the model's near-surface air temperature compares well to the NOAA-
279 CIRES-DOE Twentieth Century Reanalysis (20CR), both in terms of averages and seasonal
280 variability. The largest biases are cold temperature anomalies over the polar regions and the
281 Himalayas, and a warm anomaly over the Southern Ocean. FORTE2 simulates too little
282 rainfall compared to the 20CR, in particular over the tropical west Pacific, and the South
283 Pacific ITCZ in FORTE2 is too narrow and zonal compared to the reanalysis. While the model
284 performs well in terms of wintertime precipitation over South and East Asia, there is a dry
285 bias in the summer monsoon. Such a bias is typical for the majority of both the CMIP5 and
286 the CMIP6 ensemble (Sperber et al., 2013; Wilcox et al., 2020). The Asian summer monsoon
287 circulation is also too zonal over South East and East Asia, again consistent with the biases
288 seen in CMIP models.



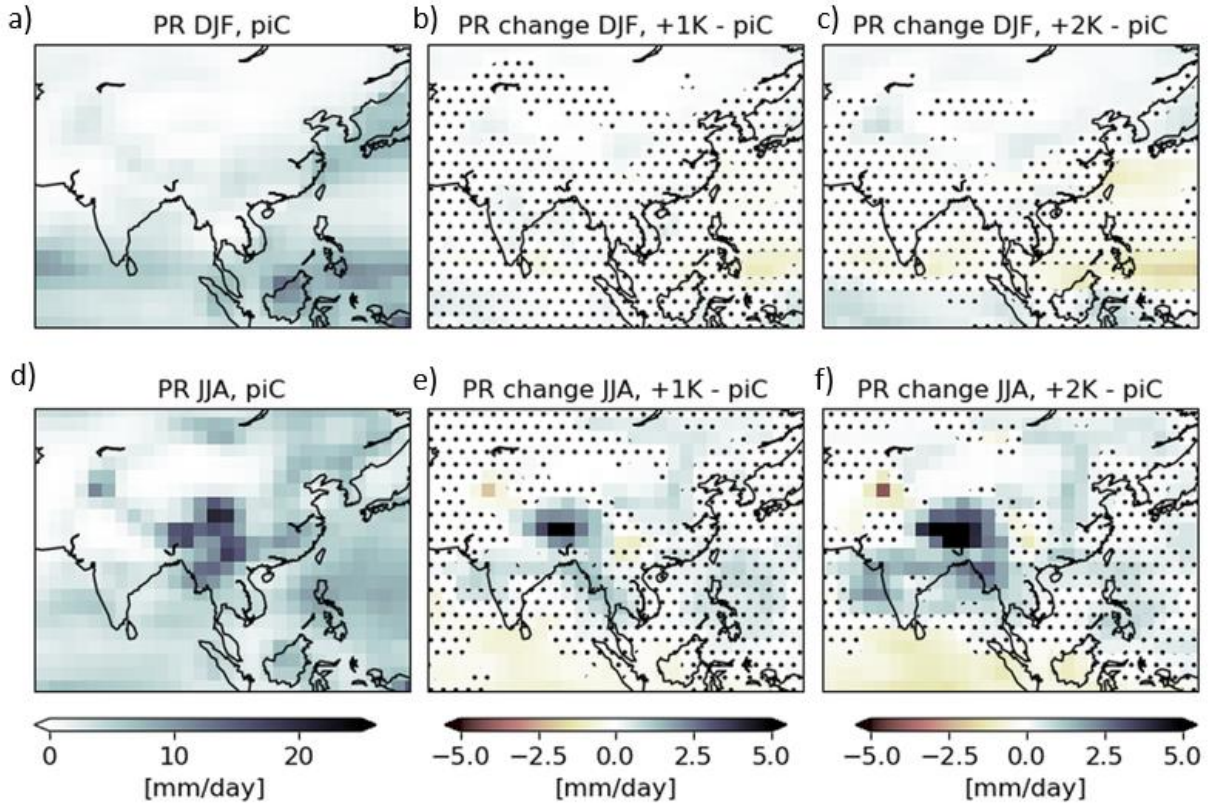
289 **Figure 3:** Baseline climatologies (for piC) of annual mean a) temperature (T) and d) precipitation (PR), as well as
290 geographical patterns of b) T and e) PR changes for +2K-piC. Rightmost panels show zonal annual mean
291 changes of c) T and f) PR. Included in the zonal precipitation panel is also the +2K-piC precipitation change
292 divided by the global mean +2K-piC temperature change (dT), illustrating the hydrological sensitivity compared
293 to +1K-piC.
294

295 The middle panels of Figure 3 show the climatological differences between +2K and piC and
296 illustrate how temperature and precipitation in FORTE2 respond to a strong increase in CO₂.
297 The 2 K global mean surface warming in FORTE2 reproduces known patterns such as an
298 Arctic amplification (Fig. 3b), seen also in the zonal mean temperature changes in Fig. 3c (in
299 the zonal panels we include differences for both +1K-piC and +2K-piC). However, this
300 warming, while causing clear responses in regional precipitation (Fig. 3e), produces a global
301 mean precipitation change of only 0.02 mm/day or 0.64 %. This gives a hydrological
302 sensitivity (HS) of merely 0.32 %/K. In comparison, energy budget constraints dictate a
303 theoretical HS of about 2 %/K (Allen and Ingram, 2002), and the CMIP6 model average HS
304 after 150 years of the 1pctCO2 simulation is 1.6 %/K (Norris et al., 2022). There are two main
305 reasons for the low FORTE2 HS. One is the low climate sensitivity, which means that the
306 relative increase in CO₂ per Kelvin of warming is high in this model. This, in turn, means that
307 the long wave absorption from CO₂ acts to mute the precipitation increase (Myhre et al.,
308 2018). The other reason is that FORTE2 has a relatively higher fraction of its rain over land,
309 where the HS is markedly lower than the global mean (Samset et al., 2018a). While the HS is
310 low, muting the absolute precipitation response to climate forcings, the overall patterns are
311 still in line with expectations when compared e.g. to CMIP6 (Tebaldi et al., 2021) or PDRMIP
312 (Samset et al., 2016) responses.

313 The dashed line in Fig. 3f shows the +2K-piC precipitation change divided by the +2K-piC
314 global mean temperature difference. As the global mean temperature change between piC
315 and +1K is by definition around 1K, we can compare the dashed and the light blue line to see
316 that the precipitation response in the two climate states (+1K and +2K) is reasonably linear.
317 There are some differences around Southern Hemisphere midlatitudes and at higher
318 Northern Hemisphere latitudes, but the zonal mean precipitation response to warming is
319 very consistent around the latitudes of the region of focus in this study. In Section 5.4 we
320 take a closer look at how aerosol responses may differ when aerosols are added at different
321 global warming levels.

322 The Asian precipitation response to +1K and +2K warming is shown in Fig. 4. In winter, there
323 is little precipitation during the winter monsoon, and the precipitation response to warming
324 is also small. In summer, global warming results in increased precipitation over most of Asia.
325 Note, however, that while Fig. 3f suggested a linear precipitation increase from +1K to +2K,

326 the geographical patterns in Fig. 4 do not show such linearity over for instance Northeast
 327 China. The pattern of the precipitation increase in +2K reflects the climatological
 328 precipitation pattern, with the maximum increase located in the region of the maximum
 329 precipitation in piC.
 330



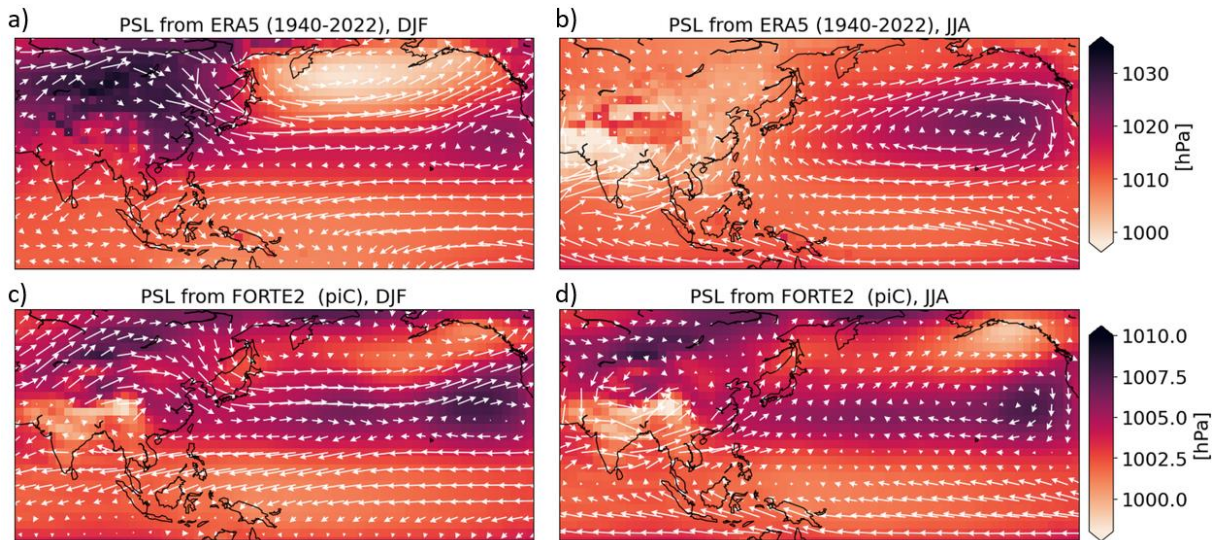
331
 332 **Figure 4:** DJF precipitation over Asia for a) piC, b) the difference between piC and +1K, and c) the difference
 333 between piC and +2K. Corresponding JJA plots are given in panels d), e) and f), respectively. Maps show
 334 averages over simulated years 51-200, and hatching indicates gridcells where the anomalies relative to piC are
 335 not significant at the 5% level.
 336

337

338 Zooming in on the region of interest in this paper, we show in Fig. 5 climatological (piC)
 339 surface pressure and 850 hPa wind for the summer (JJA) and winter (DJF) months,
 340 respectively. FORTE2 is compared to ERA5 reanalysis (Hersbach et al., 2020), averaged over
 341 the 1940-2022 period. The direction of the monsoon flow over South Asia is well captured by
 342 FORTE2. However, the flow is too weak over India and the Bay of Bengal, and is too zonal
 343 over Southeast Asia. The zonal flow over Southeast Asia, and an easterly bias in the location
 344 of the West North Pacific Subtropical High contribute to a dry bias over northeastern China.
 345 Most of the Asian summer monsoon precipitation in FORTE2 falls over Myanmar and

346 southern China (Fig 4d), while India and northeastern China are too dry. Such dry biases are
 347 common in CMIP6 models (Wilcox et al., 2020). However, the atmosphere component of
 348 FORTE, IGCM4, has been shown to reproduce the observed seasonal cycle in precipitation
 349 well (Herbert et al., 2022).

350 In winter, the Aleutian low is too weak in FORTE2 compared to ERA5. Combined with a low
 351 pressure bias over land, this causes the East Asian Winter Monsoon to also be too weak,
 352 although the direction of the flow over northeast Asia is in good agreement with the
 353 reanalysis. The seasonal variation in sea level pressure over Asia is small in FORTE2
 354 compared to ERA5, which is largely due to the pressure over land being too high in winter.
 355



356
 357 **Figure 5:** Mean sea level pressure and 850hPa winds (arrows) for ERA5 (averaged over 1940-2022) for DJF (a)
 358 and JJA (b), and for FORTE2 piC (years 51-200) for DJF (c) and JJA (c). Note that color scale limits are different
 359 between ERA5 and FORTE.
 360

361 **4.2 Pacific Ocean Response**

362 Due to the proximity of the perturbation zones to the Pacific region it is useful to assess the
 363 Pacific climatological state across the baseline climates. If differences are found between the
 364 baselines (i.e., between piC, +1K and +2K) due to different CO₂ loadings, they are likely to
 365 modify the Asian responses to regional aerosol perturbations at the different warming
 366 levels, as changes in the Pacific circulation are an important part of the response to Asian
 367 aerosol forcing (e.g., Dong et al., 2019; Wilcox et al., 2019; Williams et al., 2022).

Experiment	Niño 3 Index Standard Deviation	Niño 3.4 Index Standard Deviation	Number of El Niño Events	Number of La Niña Events
piC	0.52	0.59	15	16
+1K	0.53	0.58	17	23
+2K	0.52	0.58	16	21

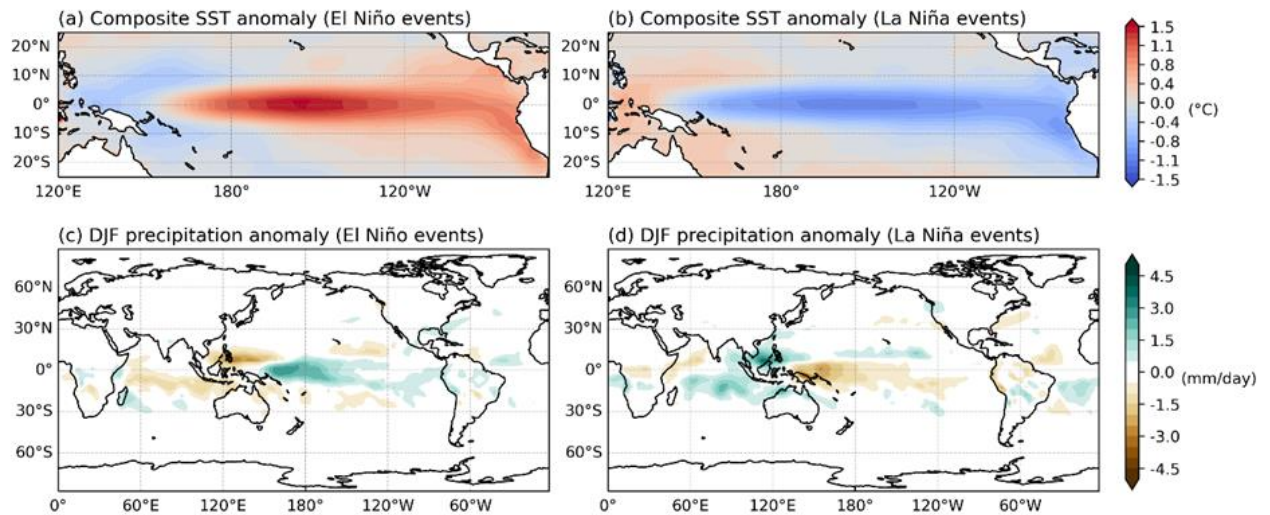
368 **Table 2:** ENSO related statistics including the two commonly used Niño regions and a breakdown of the
369 number and type of ENSO events in the three SyRAP FORTE2 baseline climates.

370

371 Standard deviations of the Niño 3.4 index are presented in Table 2 (column three) and
372 remain within a 0.1 tolerance of one another; FORTE2’s Niño 3.4 variance is on the weaker
373 end of CMIP6 models, though not an outlier (Chen et al., 2023). ENSO frequency is between
374 2 and 3 years for each baseline, which is consistent with the observed ENSO occurrence of
375 around once every 2-7 years (Allen, 2000). Table 2 demonstrates that broadly speaking,
376 variability over this key dynamical region is insensitive to changes in the global warming
377 level. Analysis is repeated for the Niño 3 index (column two) and confirms that the Pacific
378 climatological state is insensitive to CO₂ loading.

379 The large-scale SST patterns and associated winter precipitation anomalies for El Niño and La
380 Niña composites from the piC baseline are presented in Figure 6. This analysis was repeated
381 for the +1K and +2K baselines and the large-scale structures remain consistent across all
382 three baseline climates (not shown). The spatial structures of both El Niño and La Niña SST
383 composites are consistent with events captured in the Extended Reconstructed SST version
384 3b (ETSSTv3b) reanalysis over the period 1949 to 2015 (see Li et al., 2018). Notable
385 differences are: in the El Niño composite, Fig 6a, the magnitude of SST anomaly is around
386 30% weaker on the equatorial South American coastline, and in the La Niña composite the
387 cold anomaly extends too far towards the Maritime continent. Anomaly peak strength is
388 weaker than observed, around 35% and 45% weaker for the El Niño and La Niña composites
389 respectively, consistent with Blaker et al. (2021).

390



391

392 **Figure 6:** (Top Row) Composite anomalies of monthly sea surface temperature during (a) El Niño and (b) La
 393 Niña events. (Bottom Row) Winter, DJF, precipitation anomalies for (c) El Niño and (d) La Niña years.

394 Precipitation anomalies with a magnitude of less than 0.5 mm/day are in white. Data from piC baseline only.

395 Winter precipitation patterns during ENSO years are consistent with literature (Davey et al.,
 396 2014) over the Pacific and maritime continent. Expected remote precipitation impacts, such
 397 as a drying signal over southern Africa in El Niño winters (Fig. 6c) and a drying tendency
 398 stretching towards India in the La Niña winters (Fig 6d) are captured but are weak. Some
 399 remote signals, such as that over Europe, are not captured. FORTE2 is showing some
 400 promise in simulating the teleconnections associated with ENSO but this remains an active
 401 area for further investigation and model development.

402 Overall, ENSO events occur with a good frequency but are weaker than observed;
 403 particularly La Niña events are short lived and lack strength. ENSO frequency, biases and
 404 teleconnections are consistent over all three global warming levels, giving us confidence that
 405 any ENSO changes in SyRAP are primarily due to aerosol perturbations, regardless of
 406 warming level.

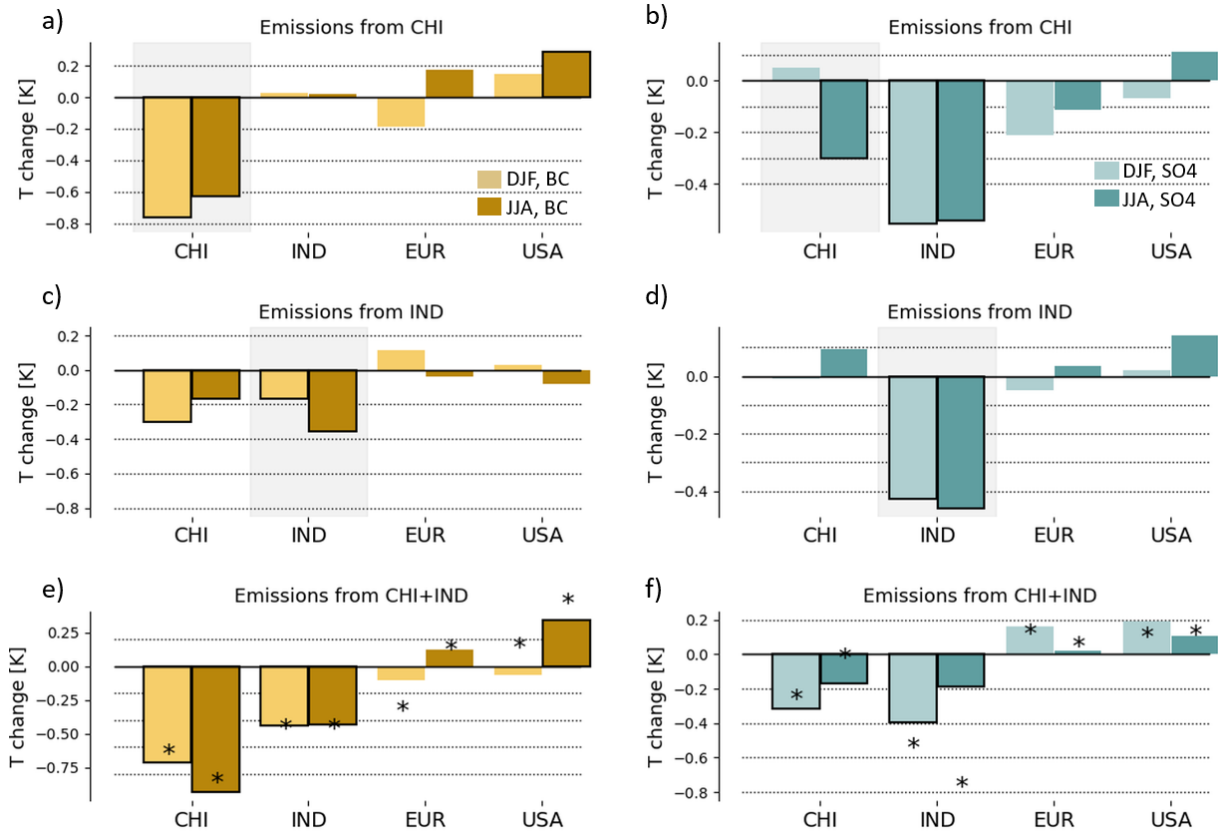
407

408 5. Results

409 5.1 Climate responses to individual aerosol perturbations

410 In both IND and CHI, the presence of BC causes strong local reductions of up to 75 Wm^{-2} in
 411 downwelling surface solar radiation at the surface (Fig. 2b,c). Similar albeit much weaker

412 reductions are seen for the SO₄ perturbations (Fig. 2e,f). These radiative perturbations
 413 trigger thermodynamic responses which manifest as (rapid) changes in near-surface
 414 temperature, surface fluxes, precipitation, and clouds, but they also influence the
 415 atmospheric circulation patterns in the region, including the Asian Summer Monsoon.

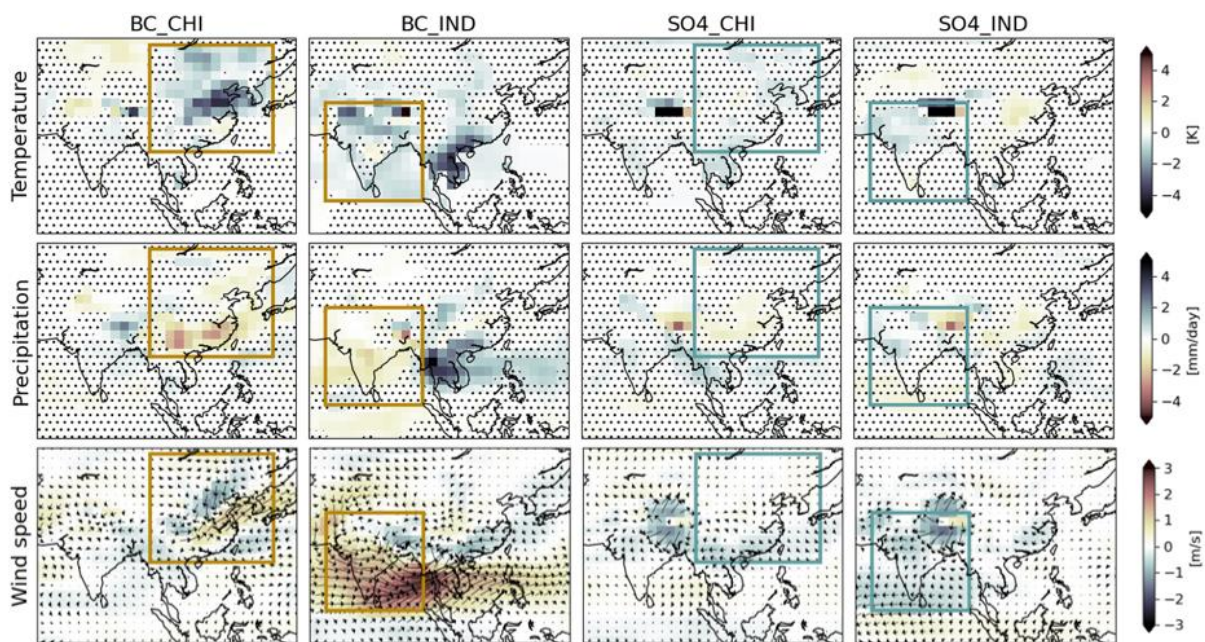


416
 417 **Figure 7:** Local (bars shaded by grey area) and remote impacts on regional mean near-surface temperature [K]
 418 in the experiments involving adding a) BC to CHI, b) SO₄ to CHI, c) BC to IND, d) SO₄ to IND, e) BC to CHI+IND
 419 and f) SO₄ to CHI+IND. Light bars show wintertime (DJF) temperature changes, while dark bars show
 420 summertime (JJA) changes. Framed bars indicate where changes are statistically significant, and star symbols in
 421 the lowermost row show the summed responses (BC_CHI + BC_IND) or (SO₄_CHI + SO₄_IND) – responses being
 422 linear where bars and stars are comparable in magnitude. We use years 51-200 of the simulation in the
 423 analysis.

424
 425 The dominant local response of adding BC or SO₄ to India or China is a statistically significant
 426 cooling (Fig. 7). The only exception is SO₄ emissions over China, which cause insignificant
 427 local warming but still trigger a strong cooling effect over India (Fig. 7b). A significant remote
 428 effect is also seen for BC over China, which causes significant summertime warming over the
 429 USA (Fig. 7a). Regional mean precipitation responses (Fig. S1) are less clear, partly because

430 the precipitation changes are not uniform in sign across the regional boxes. The regional
 431 mean precipitation responses to aerosol predominantly involve local drying, but interestingly
 432 SO₄ emissions over China cause significant local summertime precipitation increase over
 433 China, but decrease over India. Comparing precipitation responses from the CHI+IND
 434 experiment to the all-Asia perturbations of absorbing or scattering aerosols in Herbert et al.
 435 (2022), we see that both these studies find a summertime drying over India in response to
 436 absorbing aerosols over the larger region. However, while the perturbations cause a
 437 significant precipitation increase over China in Herbert et al., we find that Asian absorbing
 438 aerosols cause significant drying also over China. Similarly, SO₄ emissions over CHI+IND
 439 trigger drying over both regions in FORTE2, while Herbert et al. (2022) find scattering
 440 aerosols to cause drying over parts of India but a precipitation increase over China in IGCM4.

441



442

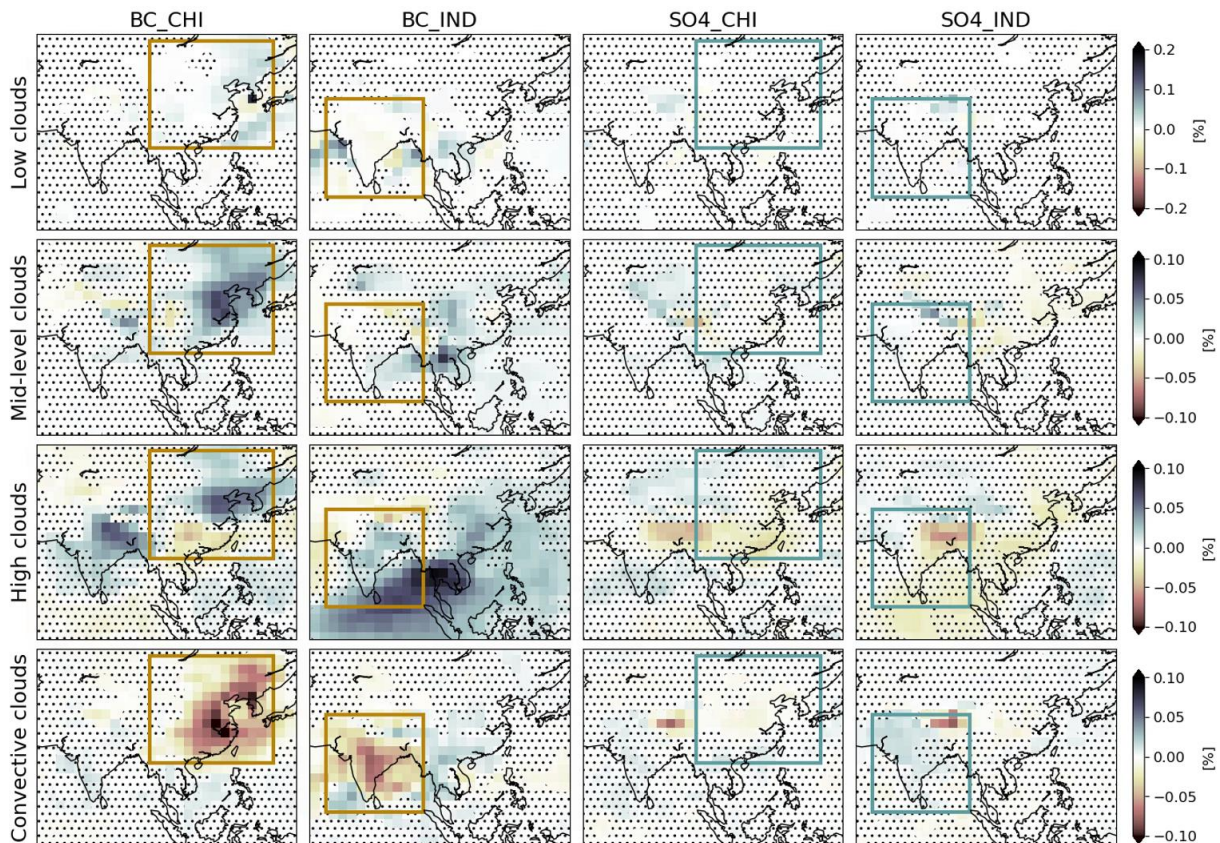
443 **Figure 8:** Mean summer (JJA) responses in near-surface temperature, precipitation and
 444 850hPa wind over the Asian region. Solid brown and blue squares mark the region where BC
 445 or SO₄ is perturbed, respectively. Maps are based on years 51-200 of the simulations, and
 446 hatched regions show areas where differences from the baseline are not statistically
 447 significant (by Student's t-test, p-value 0.05).

448

449 Figure 8 shows the geographical pattern of the summer (JJA) responses in near-surface
 450 temperature, precipitation and wind speed and direction. The addition of BC over China
 451 results in near-surface cooling, which is largely located to the north of the Yangtze river

452 (Figure 8), where the largest reductions in downwelling shortwave radiation at the surface
 453 are found (Figure 2). Precipitation south of the Yangtze decreases, associated with a strong
 454 reduction in convective cloud there (Figure 9). Adding BC over India also results in a cooling
 455 co-located with the change in AOD, but the strongest cooling in this case is seen over
 456 southeast Asia, where there is also a large increase in precipitation due to an increase in the
 457 strength of the monsoon flow from the Bay of Bengal (Figure 8). However, as in the BC_CHI
 458 case, precipitation and convective clouds decrease over the perturbation region due to the
 459 combined impact of reduced surface temperatures and increased atmospheric temperatures
 460 in response to the absorbing aerosol (see maps of temperature changes at the 850 hPa level
 461 in Fig. S2), which has a strong stabilizing effect on the atmosphere.

462



463 **Figure 9:** Mean summer (JJA) responses in low, mid-level, high and convective clouds over
 464 the Asian region. Solid brown and blue squares mark the region where BC or SO₄ is
 465 perturbed, respectively. Maps are based on years 51-200 of the simulations, and hatched
 466 regions show areas where differences from the baseline are statistically insignificant (by
 467 Student's t-test, p-value 0.05).
 468

469

470 The presence of SO_4 also cools the surface, though not as strongly as for BC for the SyRAP
471 perturbations. In SO_4 _CHI, the cooling is only significant over southeast Asia and northeast
472 Asia. Drying is seen over eastern China, but it is again weaker than in response to BC
473 increases, consistent with a weaker circulation response (Figure 8). Significant cooling is seen
474 in the northwest of the perturbation domain for SO_4 _IND, co-located with the largest
475 reductions in downwelling shortwave at the surface. This cooling results in a weaker South
476 Asian summer monsoon circulation, and a reduction in precipitation in the northwest of the
477 region (Figure 8). Precipitation and convective cloud increase in the northeast of the
478 perturbation region (Figure 9). Increasing scattering aerosol over South Asia also results in a
479 weakened East Asian summer monsoon, which results in significant warming and drying over
480 eastern China.

481 Both observations and modelling studies indicate that the drying of the Asian summer
482 monsoon seen over the past decades can be linked to increasing concentrations of
483 anthropogenic aerosols (Li et al., 2015; Liu et al., 2019; Tian et al., 2018). The SyRAP-FORTE2
484 simulations presented here allow us to decompose and understand contributions from
485 different regions or aerosol species to the total response. As shown in Section 4, FORTE2
486 reproduces the important features of Asian climate. To confirm that it also has aerosol-
487 driven climate responses consistent with more complex climate models, and thus can be
488 used to explain the decomposition of the response into the main drivers (BC vs. SO_4 or India
489 vs. China), we can compare the responses above to those from earth system model
490 simulations. Note that even among ESMs, the response to aerosol forcing varies strongly
491 between individual models, which means that we do expect there to be some differences
492 between FORTE and other studies.

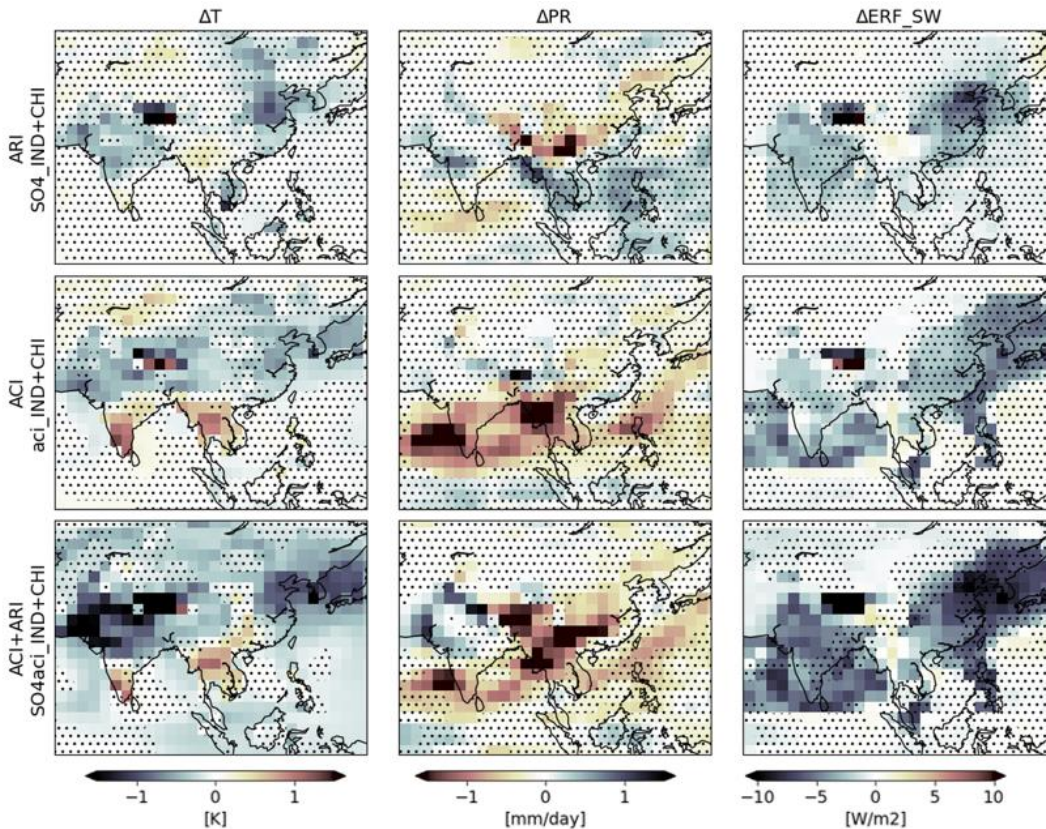
493 While most literature on the monsoon response to aerosol focuses on global all
494 anthropogenic aerosol perturbations (Salzmann et al., 2014; Song et al., 2014; Wilcox et al.,
495 2020), some regional aerosol ESM studies exist (see Section 1), for instance based on
496 PDRMIP (Xie et al., 2020; Xie et al., 2022). We find that the Asian JJA precipitation response
497 to combined India and China BC ($\text{BC}_{\text{IND+CHI}}$) is comparable to the multi-model mean
498 MJJAS response of 7 PDRMIP models to a tenfold increase of BC over Asia (Xie et al., 2020).
499 Although set-ups between these two studies are different in many aspects, including
500 different baseline climates (preindustrial versus present-day) and a much stronger

501 perturbation in the latter case, both FORTE2 and PDRMIP simulations display a BC-induced
502 increase in precipitation over India, although PDRMIP result indicate a drying over Southeast
503 Asia that we do not see. The cooling seen over India in our simulations is found in 8 out of 9
504 models in the PDRMIP simulations, but the more widespread cooling over East Asia is only
505 seen in a few of the models. Similarly, the impact of regional PDRMIP perturbations of Asian
506 SO₄ on precipitation is studied by Xie et al. (2022), who find a drying of much of the Asian
507 continent but an increase in summer precipitation over arid Central Asia. In FORTE2, the
508 sulfate response is also a drying over much of the region, but the Central Asian JJA
509 precipitation increase extends down to northern India. Recchia and Lucarini (2023) find BC
510 over China to cause local drying but wettening over India and surrounding parts of China,
511 consistent with our findings, as do Krishnamohan et al. (2021) who perform strong BC
512 perturbations in a global climate model and find that local BC enhancement causes a drying
513 over India while BC in China increases India precipitation.

514

515 **5.2 ACI responses**

516 The new ACI setup allows us to simulate the separate impacts of direct aerosol radiation
517 interactions (ARI) only (the default simulation set-up), the indirect (ACI) effect only, or the
518 simultaneous impact of both effects. Figure 10 shows the impacts of direct and indirect
519 aerosol effects on temperature, precipitation, and SW ERF. The the direct effect of sulfate
520 causes an average (over the ACI region shown in Fig. 1) SW ERF of -1.61 W/m², while the
521 indirect effect yields a response of -2.16 W/m², see Table 3. While the direct effect cools
522 most areas over Asia, the indirect effect causes a strong warming over southern parts of
523 India and the region around Thailand (Fig. 10). The contrast between direct and indirect
524 effects of Asian sulfate is particularly stark in the precipitation response (Table 3), and Fig. 10
525 shows that these differences largely originate in the regions for which the ACI trigger
526 warming.



527
 528 **Figure 10:** Summer (JJA) response to direct aerosol radiation interactions due to Asian SO₄
 529 (ARI, top row), as in the default setup in FORTE2, to aerosol-cloud interactions due to Asian
 530 SO₄ (ACI, middle row) of sulfate as represented, and both the response to Asian SO₄
 531 including both ARI and ACI (bottom row). Maps are based on years 51-200 of the
 532 simulations, and hatched regions show areas where differences from the baseline are
 533 statistically insignificant (by Student's t-test, p-value 0.05).

534

	Experiment name	Temp. [K]	Prec. [mm/day]	Surf. SW [W/m ²]	ERF_SW [W/m ²]
ARI	SO4_IND+CHI	-0.10	0.003	-1.92	-1.61
ACI	aci_IND+CHI	-0.05	-0.30	-2.98	-2.16
(ARI) + (ACI)	SO4_IND+CHI + aci_IND+CHI	-0.15	-0.303	-4.90	-3.77
ARI+ACI	SO4aci_IND+CHI	-0.35	-0.29	-4.79	-4.48
ACI_13um	aci_reff13_IND+CHI	-0.04	-0.06	-1.28	-0.87
ARI+ACI_13um	SO4aci13_reff13_IND+CHI	-0.31	-0.19	-2.73	-2.95

535 **Table 3:** Regional mean JJA impacts of the different ACI simulations, as well as the ARI only
 536 simulation (topmost table row). Changes are relative to the piC simulation and are averaged
 537 over the ACI region shown in Fig. 1.

538 Compared to the CMIP5 ensemble (Zelinka et al., 2014), FORTE2 has a similar spatial extent
539 of the ACI-driven SW forcing (see middle panel in rightmost column of Fig. 10). In CMIP5, the
540 maximum negative ACI forcing from scattering aerosols is located a bit north of Indonesia, a
541 pattern that is largely reproduced in FORTE2, albeit with a relatively strong forcing also over
542 Indian land regions. Dong et al. (2019), performing simulations with HadGEM3 with and
543 without the ACI effect, find a much more complex ACI forcing pattern, with positive SW
544 forcing over India and negative over China. In terms of the relative importance of ACI versus
545 ARI, both (Zelinka et al., 2014) and Dong et al. (2019) are consistent with the present study
546 in that ACI exert the strongest radiative impact in the region. Dong et al. (2019) found that
547 ARI resulted in weak circulation and precipitation changes, and that ACI was the dominant
548 driver of monsoon changes. An important part of this mechanism, however, was the ACI-
549 induced warming in Maritime Continent SST, which is not something we see in FORTE2. The
550 precipitation response pattern of Dong et al. (2019) is also very different from FORTE2, with
551 an increase in South Asian and and decrease in East Asian precipitation. The comparison of
552 Guo et al. (2015) showing differences in Asian precipitation patterns between CMIP5 models
553 with and without ACI, however, is more consistent with FORTE2 results. The nine CMIP5
554 models with only ARI show a drying over China and increased precipitation over India, while
555 the models including ACI give a drying over both India and China, similar to what we find
556 here (Fig. 10).

557 The clean separation into simulations with ARI-only, ACI-only and both ARI and ACI allows for
558 an assessment of the linearity of these two processes. Looking at the regional means in
559 Table 3, comparing the sum of ARI and ACI (see row “(ARI) + (ACI)”) to the experiment
560 including both processes (“ARI+ACI”), we find that while precipitation and downwelling
561 shortwave radiation are close to linear, temperature is not. By closer inspection, this
562 nonlinearity originates from the northernmost latitudes of this region, for which ARI or ACI
563 individually cause warming, but which cools when both ARI and ACI operate simultaneously
564 (Fig. 10). Remote impacts of including the ACI effect, as well as nonlinearities, can be seen in
565 the global maps in Fig. S3. For instance, while both the ARI and ACI effects cause a similar
566 pattern of remote warming over the eastern parts of USA and Canada, the combined impact
567 of these effects does not include such a warming (compare lower two rows of Fig. S3). Likely,

568 the “double” kick to the system is strong enough to trigger a different set of circulation
569 responses including a more unified cooling over the entire North American region.

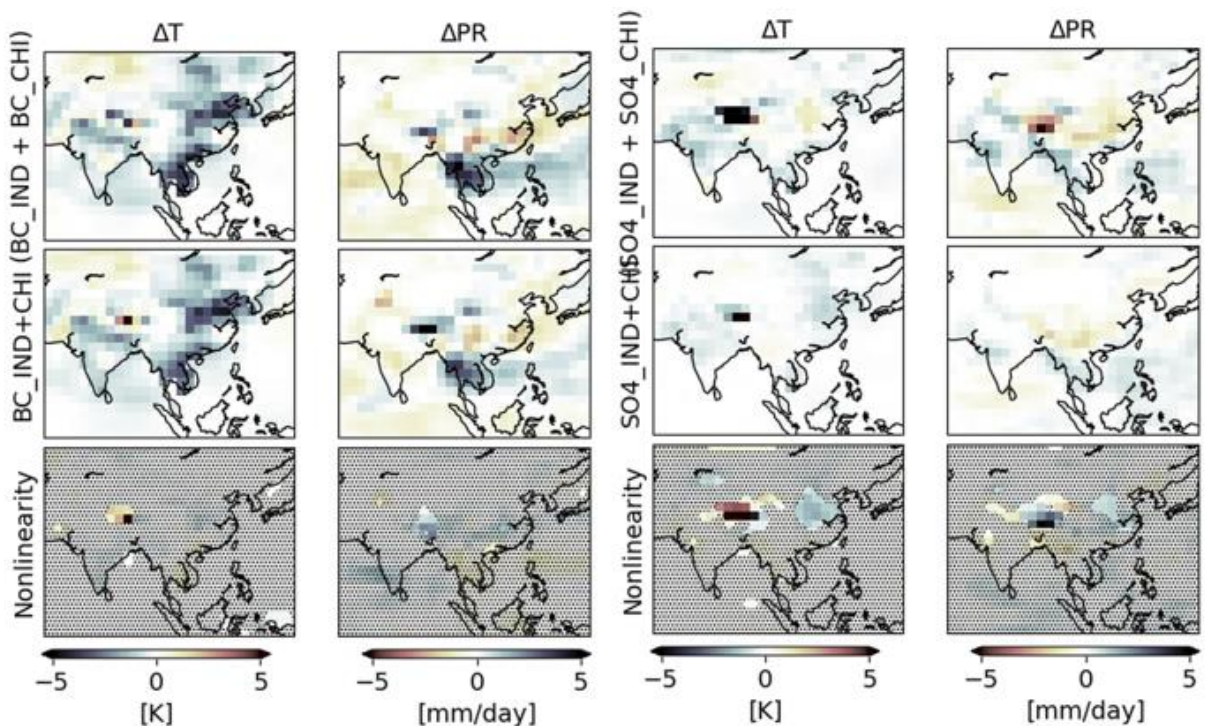
570 The SyRAP-FORTE2 setup also allows for testing how important the uncertainty in ACI is for
571 the simulated response to aerosol forcing in this region. In the present study, we have tested
572 the sensitivity to the emulated aerosol-induced cloud radius reduction (which in the default
573 setup is reduced from 15 to 10 μm) by performing additional experiments only reducing the
574 droplet radius to 13 μm . Although the relative droplet radius reduction change between
575 default ACI and sensitivity ACI experiments is only 2 μm , the radiative impacts (Surf. SW and
576 ERF_SW in Table 3) are almost halved. Though a large difference, this is not necessarily
577 unrealistic, as the effect on radiation tends not to scale linearly with effective cloud radius
578 (Boers and Rotstayn, 2001). While we also find that the difference in ACI impact on
579 precipitation between these two experiments is substantial, the temperature change is
580 almost the same between the experiments (-0.05 K for the default ACI experiment, and -0.04
581 K for the sensitivity experiment). We also note that the difference in precipitation impacts
582 from ARI+ACI in default versus sensitivity setup is much smaller than when comparing only
583 ACI impacts. Clearly, many nonlinear processes are involved between an initial droplet
584 change, the radiative impact and resulting changes to meteorological variables.

585

586 **5.3 Regional linearity of the perturbations**

587 There are many examples of idealized model simulations of regional aerosol perturbations in
588 the literature, and some of these studies have investigated the regional linearity or additivity
589 of the climate responses. A recent example is Herbert et al. (2022), who used the
590 atmospheric component of FORTE2 and performed separate simulations removing BC or SO₄
591 from India or China. In stark contrast to our results, they find strongly nonlinear responses in
592 the summer monsoon precipitation. Chen et al. (2020) also conclude, after comparing
593 regional climate model simulations adding BC to India, China or both combined, that
594 responses to BC are highly nonlinear. In contrast, Recchia and Lucarini (2023), also using a
595 reduced-complexity model, find relatively linear responses in idealized experiments
596 emulating the addition of BC aerosols over India, China, and Southeast Asia separately or at
597 once.

598 Here, we investigate the regional linearity in BC/SO₄ perturbations by comparing the added
 599 impacts of BC/SO₄ perturbations over IND and CHI to experiments where we perturb BC/SO₄
 600 over both regions at once. The bottom row of Fig. 11 (left half) illustrates the nonlinearity to
 601 BC perturbations in the two regions. Positive values mean that adding BC to both regions at
 602 once triggers a stronger response than the sum of responses when adding BC to the two
 603 regions individually. As indicated by the hatchings in Fig. 11, the regional BC perturbations
 604 are significantly nonlinear only in a very small region in Northern India. As can be seen by
 605 comparing the individual maps, this region is typically a transitional region between different
 606 climate responses. It is also a region of complex topography, and Herbert et al. (2022)
 607 showed that different circulation patterns interacting with the orography was a key factor
 608 for the nonlinearity of the response.



609
 610 **Figure 11:** The linearity of mean summer (JJA) temperature and precipitation responses to
 611 BC and SO₄. Topmost row shows the sum of the responses from the individual regional
 612 experiments, middle row show responses from an experiment where aerosol is added to
 613 both IND and CHI at once, and bottom row shows the difference between the two above,
 614 thus quantifying the nonlinearity. Maps are based on years 51-200 of the simulations, and
 615 grid cells with statistically significant nonlinearity are indicated by absence of hatchings.

616

617 Nonlinearities in responses to SO₄ (right half of Fig. 11) are slightly larger than for BC.

618 Significant nonlinearities are, like for BC, present over parts of Northern India, but also over
 619 China around the same latitudes. In particular, when SO₄ is added to both CHI and IND at

620 once (middle row) there is a small cooling over China not present in the added responses
621 (first row). Looking back at Fig. 8 (upper right corner panel) we see that adding SO₄ to India
622 alone caused a statistically significant warming over China, and this warming is associated
623 with a region of significant anomalous descent (not shown) and reduction in mid-level clouds
624 (Fig. 9). To summarize, some processes are only evident when particularly SO₄ is added to a
625 specific region, and not necessarily when adjacent regions are cooled by SO₄
626 simultaneously. In general, however, responses to both BC and SO₄ in FORTE2 are
627 reasonably linear.

628 As IGCM4 used by Herbert et al. (2022) is FORTE's atmospheric component, their much
629 stronger nonlinearity is surprising. One possible cause of this disparity could be the
630 substantially larger spatial extent of our forcing. To test this, we performed an additional
631 version of the IND experiment where the IND region was limited to the Northern parts of
632 India only, more similar to Herbert et al. (Table 1). Compare black dashed (IND) and light
633 grey dotted line (NIND) in Fig. 1. However, as seen in Figure S4, results are no less linear with
634 this smaller perturbation region. Instead, this discrepancy might arise from the fact that our
635 simulations are fully coupled to an ocean model, or it may be related to the simulation
636 design (for instance, Herbert et al. (2022) remove aerosols from a present-day climate and
637 aerosols field, while we add aerosols to a preindustrial climate with no aerosols). Either way,
638 the linearity allows for the utilization of these simulations in an additive manner.

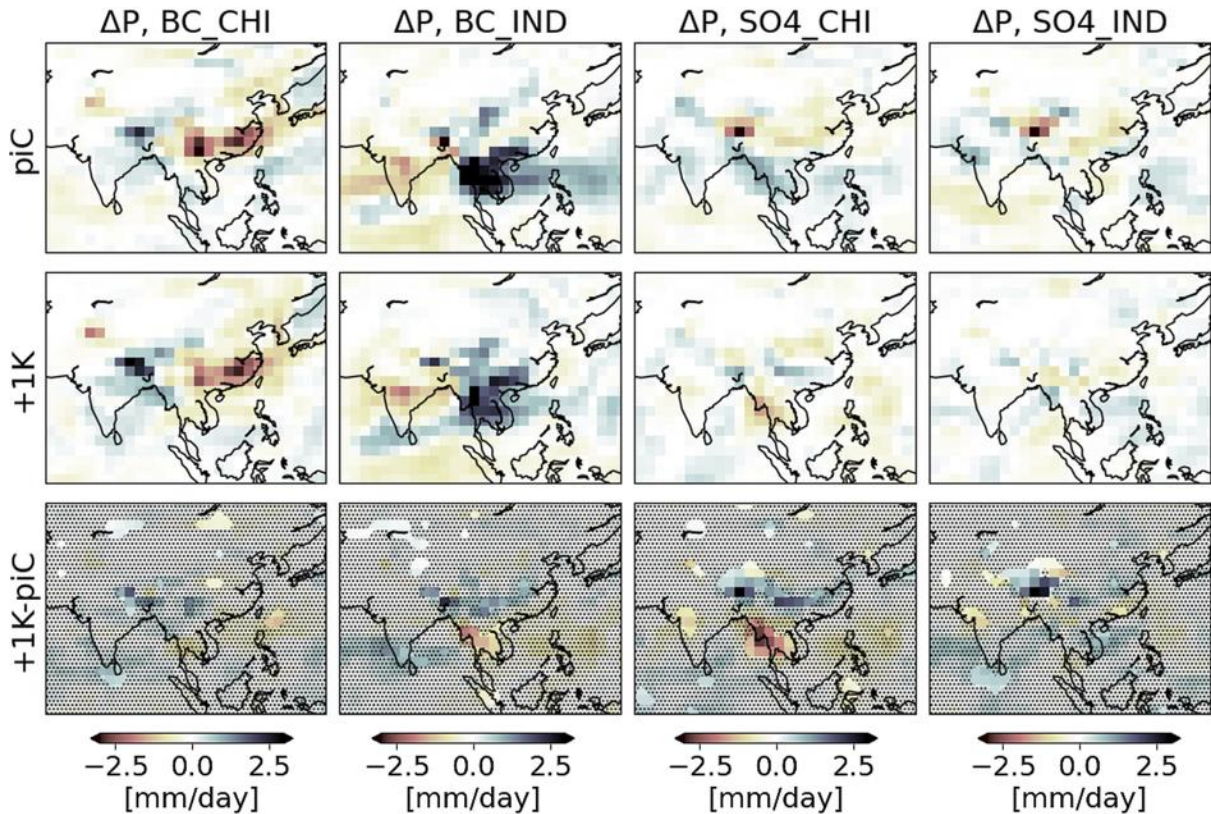
639 **5.4 Aerosol impacts on Asian climate for different climate states**

640 In the core simulations presented in Section 3, aerosols were perturbed on top of a
641 preindustrial climate (piC) in terms of CO₂ levels (280 ppmv). However, in both the present-
642 day as well as the future, the climate will be in a different state, notably with higher
643 concentrations of CO₂ and higher average temperatures. In a separate set of simulations, we
644 have investigated how the Asian climate responds to BC and SO₄ aerosols on top of a climate
645 that is one degree warmer (+1K; CO₂ level at 500 ppmv) than in our core simulations.
646 Comparing these sets of simulations allows an assessment of whether different climate
647 responses to aerosols can be expected to emerge as climate warms.

648 In general, BC aerosols cause similar geographical precipitation response patterns as climate
649 warms (compare rows in the leftmost half of Fig. 12). The lowermost row indicates that
650 adding BC to China in the different climates does not lead to significant differences in

651 precipitation responses in any widespread subregions, while adding BC to India leads to a
 652 significantly weaker precipitation increase over Myanmar and Thailand in the warmer
 653 climate.

654



655

656 **Figure 12:** Mean summer (JJA) responses in precipitation in a preindustrial climate (upper
 657 row), a 1 degree warmer climate (middle row) and the difference between the two (bottom
 658 row). Maps are based on years 51-200 of the simulations, and hatching indicates where the
 659 difference between the aerosol responses in the two different climates are not statistically
 660 significant.

661

662 In both SO_4 experiments, we see stronger differences in the precipitation response between
 663 the different climates. Adding SO_4 over India causes a drying over the Himalayas and the
 664 south tip of India in the preindustrial climate but not in the warmer climate. A similar effect
 665 in the Himalayan region can be seen for SO_4 over China, but the starkest difference is found
 666 over Myanmar and Thailand. In the preindustrial climate the Indian SO_4 triggers a
 667 precipitation increase, while in the warmer climate the signal changes sign and becomes a
 668 drying. This sensitivity of the SO_4 response to the background climate underlines the
 669 importance of the simulation setup when studying aerosol-climate interactions, and also
 670 how inferences drawn about sensitivities to aerosol emissions in today's climate may not

671 hold for future levels of global warming. This remains a largely unquantified source of
672 uncertainty in future projections of aerosol emission influences.

673

674 **6. Conclusions**

675 Aerosol climate impacts can follow patterns and time evolutions that are different to those
676 from greenhouse gas driven global surface warming, potentially enhancing climate risk when
677 combined with regionally differing socioeconomic factors. However, our understanding of
678 these aerosol specific patterns and processes is still limited. For instance, in Asia, a high
679 population density in combination with high water stress makes the region vulnerable, in
680 particular to changes in precipitation. Recognizing this vulnerability, many previous model
681 studies have analyzed impacts of different types of aerosols from different Asian subregions,
682 studied the role of direct versus indirect aerosol effects, or explored how specific aerosol
683 impacts change in a changing climate.

684 In this work, using a reduced-complexity climate model, we address all these processes,
685 allowing for a comparison of the relative importance of the different effects. We have shown
686 how a set of systematic aerosol emission perturbations in a reduced-complexity climate
687 model can be used to identify physical responses to regionalized aerosol emissions, with a
688 range of physical properties, and that it is possible to combine these into a tool for building
689 hypotheses about the joint influence of baskets of aerosol emission types.

690 We found that perturbations of absorbing or scattering aerosols in FORTE2 reproduce
691 important features already shown in the literature, based on observations, and on
692 simulations using more complex earth system models. We find that the presence of black
693 carbon (BC) and sulfate (SO_4) aerosols in China and India cause local reductions in surface
694 solar radiation that trigger thermodynamic responses, leading to changes in temperature,
695 surface fluxes and precipitation. The dynamical responses in pressure, winds, and circulation
696 patterns contribute to changes in clouds and precipitation and have widespread impacts
697 outside the perturbed areas. Adding BC over China causes a strong local precipitation
698 reduction. BC over India also causes local drying but a strong increase in precipitation over
699 Southeast Asia. Adding SO_4 over China leads to reduced precipitation locally, while SO_4 over

700 India leads to increased precipitation in northwestern India and warming and drying over
701 East China.

702 The same amount of BC or SO₄ aerosols cause weaker near-surface cooling and precipitation
703 changes in a warmer climate. However, the geographical distribution of precipitation
704 changes on a sub-regional scale reveal important differences. For instance, SO₄ over China
705 causes increased precipitation over Southeast Asia in a preindustrial climate, but in a
706 warmer climate, the precipitation impact of SO₄ on this region changes sign entirely.

707 Adding the separate response to a given aerosol impact in the two different regions (IND and
708 CHI) are comparable to the impact of adding aerosols to both regions at once. In other
709 words, responses are reasonably linear, which makes the SyRAP simulations well suited as a
710 tool for understanding joint influences of multiple aerosol-driven climate forcings. While the
711 focus of our work has been on Asia, and the regions home to the current dominant emitters
712 of anthropogenic aerosols, similar studies for other regions would be highly useful as a
713 future exercise. They could also include the responses to natural aerosol sources such as
714 dust, biomass burning and sea salt, expected to become more important as we transition
715 into a post-fossil future with a warmer global climate.

716

717 **Acknowledgements**

718 We acknowledge the Center for Advanced Study in Oslo, Norway that funded and hosted our
719 HETCLIF centre during the academic year of 2023/24. The research presented in this paper
720 was carried out on the high-performance computing cluster supported by the Research and
721 Specialist Computing Support service at the University of East Anglia, UK. Data were stored
722 and shared on project account NS9042KK on resources provided by UNINETT Sigma2 – the
723 National Infrastructure for High Performance Computing and Data Storage in Norway. All
724 coauthors were supported by the Research Council of Norway [Grant no. 324182 (CA³THY)].

725

726

727 **Data availability statement**

728 The present analyses is based on model simulations using the FORTE2 (version v2.0)
729 reduced-complexity climate model . The model is freely available for download at
730 <https://zenodo.org/records/3632569>. Aerosol perturbation simulations use aerosol optical
731 depth from the CAMSRA, as detailed in the Methods section. The Copernicus Atmosphere
732 Monitoring Reanalysis (CAMSRA) was downloaded from the Copernicus Atmosphere
733 Monitoring Service (CAMS) Atmosphere Data Store (ADS)
734 [https://ads.atmosphere.copernicus.eu/cdsapp#!/dataset/cams-global-reanalysis-
735 eac4?tab=overview](https://ads.atmosphere.copernicus.eu/cdsapp#!/dataset/cams-global-reanalysis-eac4?tab=overview). Figure 5 compares FORTE2 sea level pressure and winds to that from
736 ERA5 reanalysis (Hersbach et al., 2020), which is available for download here:

737 <https://cds.climate.copernicus.eu/cdsapp#!/dataset/reanalysis-era5-single->
738 [levels?tab=overview](https://cds.climate.copernicus.eu/cdsapp#!/dataset/reanalysis-era5-single-levels?tab=overview). All FORTE2 model results are available for download at the repository
739 <https://archive.sigma2.no/>, at
740 <https://archive.norstore.no/pages/public/datasetDetail.jsf?id=10.11582/2023.00140> [data
741 are currently awaiting a DOI and will be available at <https://doi.org/xxxx>]. Python code for
742 analysis of the FORTE2 results as well as for plotting figures in the manuscript will be
743 available for download at the same repository.
744

745 References

- 746 Allen, M. R., and Ingram, W. J.: Constraints on future changes in climate and the hydrologic
747 cycle, *Nature*, 419, 228-232, 10.1038/nature01092, 2002.
- 748 Allen, R. J.: ENSO: Multiscale Variability and Global and Regional Impacts, Cambridge Univ.
749 Press, New York, 2000.
- 750 Blaker, A. T., Joshi, M., Sinha, B., Stevens, D. P., Smith, R. S., and Hirschi, J. J. M.: FORTE
751 2.0: a fast, parallel and flexible coupled climate model, *Geosci. Model Dev.*, 14, 275-293,
752 10.5194/gmd-14-275-2021, 2021.
- 753 Boers, R., and Rotstayn, L. D.: Possible links between cloud optical depth and effective
754 radius in remote sensing observations, *Quarterly Journal of the Royal Meteorological*
755 *Society*, 127, 2367-2383, <https://doi.org/10.1002/qj.49712757709>, 2001.
- 756 Bollasina, M. A., Ming, Y., and Ramaswamy, V.: Anthropogenic Aerosols and the Weakening
757 of the South Asian Summer Monsoon, *Science*, 334, 502-505, doi:10.1126/science.1204994,
758 2011.
- 759 Chen, H., Zhuang, B., Liu, J., Li, S., Wang, T., Xie, X., Xie, M., Li, M., and Zhao, M.: Regional
760 Climate Responses in East Asia to the Black Carbon Aerosol Direct Effects from India and
761 China in Summer, *Journal of Climate*, 33, 9783-9800, [https://doi.org/10.1175/JCLI-D-19-](https://doi.org/10.1175/JCLI-D-19-0706.1)
762 [0706.1](https://doi.org/10.1175/JCLI-D-19-0706.1), 2020.
- 763 Chen, S., Chen, W., Yu, B., and Wu, R.: How Well Can Current Climate Models Simulate the
764 Connection of the Early Spring Aleutian Low to the Following Winter ENSO?, *Journal of*
765 *Climate*, 36, 603-624, <https://doi.org/10.1175/JCLI-D-22-0323.1>, 2023.
- 766 Chen, W., Dong, B., Wilcox, L., Luo, F., Dunstone, N., and Highwood, E. J.: Attribution of
767 Recent Trends in Temperature Extremes over China: Role of Changes in Anthropogenic
768 Aerosol Emissions over Asia, *Journal of Climate*, 32, 7539-7560, 10.1175/jcli-d-18-0777.1,
769 2019.
- 770 Cook, J., and Highwood, E. J.: Climate response to tropospheric absorbing aerosols in an
771 intermediate general-circulation model, *Quarterly Journal of the Royal Meteorological*
772 *Society*, 130, 175-191, <https://doi.org/10.1256/qj.03.64>, 2004.
- 773 Davey, M. K., Brookshaw, A., and Ineson, S.: The probability of the impact of ENSO on
774 precipitation and near-surface temperature, *Climate Risk Management*, 1, 5-24,
775 <https://doi.org/10.1016/j.crm.2013.12.002>, 2014.
- 776 Dong, B., Sutton, R. T., Highwood, E. J., and Wilcox, L. J.: Preferred response of the East
777 Asian summer monsoon to local and non-local anthropogenic sulphur dioxide emissions,
778 *Climate Dynamics*, 46, 1733-1751, 10.1007/s00382-015-2671-5, 2016.
- 779 Dong, B., Wilcox, L. J., Highwood, E. J., and Sutton, R. T.: Impacts of recent decadal
780 changes in Asian aerosols on the East Asian summer monsoon: roles of aerosol–radiation
781 and aerosol–cloud interactions, *Climate Dynamics*, 53, 3235-3256, 10.1007/s00382-019-
782 04698-0, 2019.
- 783 Fan, J., Rosenfeld, D., Yang, Y., Zhao, C., Leung, L. R., and Li, Z.: Substantial contribution
784 of anthropogenic air pollution to catastrophic floods in Southwest China, *Geophysical*
785 *Research Letters*, 42, 6066-6075, <https://doi.org/10.1002/2015GL064479>, 2015.
- 786 Ferraro, A. J., Highwood, E. J., and Charlton-Perez, A. J.: Weakened tropical circulation and
787 reduced precipitation in response to geoengineering, *Environmental Research Letters*, 9,
788 014001, 10.1088/1748-9326/9/1/014001, 2014.

789 Forster, P., T. Storelvmo, K. Armour, W. Collins, J.-L. Dufresne, D. Frame, D.J. Lunt, T.
790 Mauritsen, M.D. Palmer, M. Watanabe, M. Wild, and H. Zhang: The Earth's Energy Budget,
791 Climate Feedbacks, and Climate Sensitivity. , in: The Physical Science Basis. Contribution of
792 Working Group I to the Sixth Assessment Report of the Intergovernmental Panel on Climate
793 Change, edited by: Masson-Delmotte, V., P. Zhai, A. Pirani, S.L. Connors, C. Péan, S.
794 Berger, N. Caud, Y. Chen, L. Goldfarb, M.I. Gomis, M. Huang, K. Leitzell, E. Lonnoy, J.B.R.
795 Matthews, T.K. Maycock, T. Waterfield, O. Yelekçi, R. Yu, and B. Zhou, Cambridge
796 University Press, Cambridge, United Kingdom and New York, NY, USA, pp. 923–1054, 2021.
797 Forster, P. M., Blackburn, M., Glover, R., and Shine, K. P.: An examination of climate
798 sensitivity for idealised climate change experiments in an intermediate general circulation
799 model, *Climate Dynamics*, 16, 833-849, 10.1007/s003820000083, 2000.
800 Giorgi, F., and Gao, X.-J.: Regional earth system modeling: review and future directions,
801 *Atmospheric and Oceanic Science Letters*, 11, 189-197, 10.1080/16742834.2018.1452520,
802 2018.
803 Granier, C., Bessagnet, B., Bond, T., D'Angiola, A., Denier van der Gon, H., Frost, G. J.,
804 Heil, A., Kaiser, J. W., Kinne, S., Klimont, Z., Kloster, S., Lamarque, J.-F., Liousse, C., Masui,
805 T., Meleux, F., Mieville, A., Ohara, T., Raut, J.-C., Riahi, K., Schultz, M. G., Smith, S. J.,
806 Thompson, A., van Aardenne, J., van der Werf, G. R., and van Vuuren, D. P.: Evolution of
807 anthropogenic and biomass burning emissions of air pollutants at global and regional scales
808 during the 1980–2010 period, *Climatic Change*, 109, 163, 10.1007/s10584-011-0154-1,
809 2011.
810 Guo, L., Turner, A. G., and Highwood, E. J.: Impacts of 20th century aerosol emissions on
811 the South Asian monsoon in the CMIP5 models, *Atmos. Chem. Phys.*, 15, 6367-6378,
812 10.5194/acp-15-6367-2015, 2015.
813 Guo, Y., Dong, B., and Zhu, J.: Anthropogenic impacts on changes in summer extreme
814 precipitation over China during 1961–2014: roles of greenhouse gases and anthropogenic
815 aerosols, *Climate Dynamics*, 10.1007/s00382-022-06453-4, 2022.
816 Herbert, R., Wilcox, L. J., Joshi, M., Highwood, E., and Frame, D.: Nonlinear response of
817 Asian summer monsoon precipitation to emission reductions in South and East Asia,
818 *Environmental Research Letters*, 17, 014005, 10.1088/1748-9326/ac3b19, 2022.
819 Hersbach, H., Bell, B., Berrisford, P., Hirahara, S., Horányi, A., Muñoz-Sabater, J., Nicolas,
820 J., Peubey, C., Radu, R., Schepers, D., Simmons, A., Soci, C., Abdalla, S., Abellan, X.,
821 Balsamo, G., Bechtold, P., Biavati, G., Bidlot, J., Bonavita, M., De Chiara, G., Dahlgren, P.,
822 Dee, D., Diamantakis, M., Dragani, R., Flemming, J., Forbes, R., Fuentes, M., Geer, A.,
823 Haimberger, L., Healy, S., Hogan, R. J., Hólm, E., Janisková, M., Keeley, S., Lalouaux, P.,
824 Lopez, P., Lupu, C., Radnoti, G., de Rosnay, P., Rozum, I., Vamborg, F., Villaume, S., and
825 Thépaut, J.-N.: The ERA5 global reanalysis, *Quarterly Journal of the Royal Meteorological
826 Society*, 146, 1999-2049, <https://doi.org/10.1002/qj.3803>, 2020.
827 Highwood, E. J., and Stevenson, D. S.: Atmospheric impact of the 1783–1784 Laki Eruption:
828 Part II Climatic effect of sulphate aerosol, *Atmos. Chem. Phys.*, 3, 1177-1189, 10.5194/acp-
829 3-1177-2003, 2003.
830 Holben, B. N., Eck, T. F., Slutsker, I., Tanré, D., Buis, J. P., Setzer, A., Vermote, E., Reagan,
831 J. A., Kaufman, Y. J., Nakajima, T., Lavenu, F., Jankowiak, I., and Smirnov, A.: AERONET—
832 A Federated Instrument Network and Data Archive for Aerosol Characterization, *Remote
833 Sensing of Environment*, 66, 1-16, [https://doi.org/10.1016/S0034-4257\(98\)00031-5](https://doi.org/10.1016/S0034-4257(98)00031-5), 1998.
834 Inness, A., Ades, M., Agustí-Panareda, A., Barré, J., Benedictow, A., Blechschmidt, A. M.,
835 Dominguez, J. J., Engelen, R., Eskes, H., Flemming, J., Huijnen, V., Jones, L., Kipling, Z.,
836 Massart, S., Parrington, M., Peuch, V. H., Razinger, M., Remy, S., Schulz, M., and Suttie, M.:
837 The CAMS reanalysis of atmospheric composition, *Atmos. Chem. Phys.*, 19, 3515-3556,
838 10.5194/acp-19-3515-2019, 2019.
839 CAMS global reanalysis (EAC4) monthly averaged fields.:
840 [https://ads.atmosphere.copernicus.eu/cdsapp#!/dataset/cams-global-reanalysis-eac4-
841 monthly?tab=overview](https://ads.atmosphere.copernicus.eu/cdsapp#!/dataset/cams-global-reanalysis-eac4-monthly?tab=overview), 2019.

842 Joshi, M., Stringer, M., van der Wiel, K., O'Callaghan, A., and Fueglistaler, S.: IGCM4: a fast,
843 parallel and flexible intermediate climate model, *Geosci. Model Dev.*, 8, 1157-1167,
844 10.5194/gmd-8-1157-2015, 2015.

845 Kaiser, J. W., Heil, A., Andreae, M. O., Benedetti, A., Chubarova, N., Jones, L., Morcrette, J.
846 J., Razinger, M., Schultz, M. G., Suttie, M., and van der Werf, G. R.: Biomass burning
847 emissions estimated with a global fire assimilation system based on observed fire radiative
848 power, *Biogeosciences*, 9, 527-554, 10.5194/bg-9-527-2012, 2012.

849 Krishnamohan, K. S., Modak, A., and Bala, G.: Effects of local and remote black carbon
850 aerosols on summer monsoon precipitation over India, *Environmental Research
851 Communications*, 3, 081003, 10.1088/2515-7620/ac18d1, 2021.

852 Levy, R. C., Mattoo, S., Munchak, L. A., Remer, L. A., Sayer, A. M., Patadia, F., and Hsu, N.
853 C.: The Collection 6 MODIS aerosol products over land and ocean, *Atmos. Meas. Tech.*, 6,
854 2989-3034, 10.5194/amt-6-2989-2013, 2013.

855 Li, B., Ding, R., Li, J., Xu, Y., and Li, J.: Asymmetric Response of Predictability of East Asian
856 Summer Monsoon to ENSO, *SOLA*, 14, 52-56, 10.2151/sola.2018-009, 2018.

857 Li, J., Carlson, B. E., Yung, Y. L., Lv, D., Hansen, J., Penner, J. E., Liao, H., Ramaswamy,
858 V., Kahn, R. A., Zhang, P., Dubovik, O., Ding, A., Lacis, A. A., Zhang, L., and Dong, Y.:
859 Scattering and absorbing aerosols in the climate system, *Nature Reviews Earth &
860 Environment*, 3, 363-379, 10.1038/s43017-022-00296-7, 2022.

861 Li, X., Ting, M., Li, C., and Henderson, N.: Mechanisms of Asian Summer Monsoon Changes
862 in Response to Anthropogenic Forcing in CMIP5 Models, *Journal of Climate*, 28, 4107-4125,
863 <https://doi.org/10.1175/JCLI-D-14-00559.1>, 2015.

864 Liu, J., Rühland, K. M., Chen, J., Xu, Y., Chen, S., Chen, Q., Huang, W., Xu, Q., Chen, F.,
865 and Smol, J. P.: Aerosol-weakened summer monsoons decrease lake fertilization on the
866 Chinese Loess Plateau, *Nature Climate Change*, 7, 190-194, 10.1038/nclimate3220, 2017.

867 Liu, Y., Cai, W., Sun, C., Song, H., Cobb, K. M., Li, J., Leavitt, S. W., Wu, L., Cai, Q., Liu, R.,
868 Ng, B., Cherubini, P., Büntgen, U., Song, Y., Wang, G., Lei, Y., Yan, L., Li, Q., Ma, Y., Fang,
869 C., Sun, J., Li, X., Chen, D., and Linderholm, H. W.: Anthropogenic Aerosols Cause Recent
870 Pronounced Weakening of Asian Summer Monsoon Relative to Last Four Centuries,
871 *Geophysical Research Letters*, 46, 5469-5479, <https://doi.org/10.1029/2019GL082497>, 2019.

872 Myhre, G., Forster, P. M., Samset, B. H., Hodnebrog, Ø., Sillmann, J., Aalbergstjø, S. G.,
873 Andrews, T., Boucher, O., Faluvegi, G., Fläschner, D., Kasoar, M., Kharin, V., Kirkevåg, A.,
874 Lamarque, J.-F., Olivié, D., Richardson, T., Shindell, D., Shine, K. P., Stjern, C. W.,
875 Takemura, T., Voulgarakis, A., and Zwiers, F.: PDRMIP: A Precipitation Driver and
876 Response Model Intercomparison Project, Protocol and preliminary results, *Bulletin of the
877 American Meteorological Society*, 98, 1185-1198, doi: 10.1175/BAMS-D-16-0019.1, 2017.

878 Myhre, G., Kramer, R. J., Smith, C. J., Hodnebrog, Ø., Forster, P., Soden, B. J., Samset, B.
879 H., Stjern, C. W., Andrews, T., Boucher, O., Faluvegi, G., Fläschner, D., Kasoar, M.,
880 Kirkevåg, A., Lamarque, J.-F., Olivié, D., Richardson, T., Shindell, D., Stier, P., Takemura, T.,
881 Voulgarakis, A., and Watson-Parris, D.: Quantifying the Importance of Rapid Adjustments for
882 Global Precipitation Changes, *Geophysical Research Letters*, 45, 11,399-311,405,
883 <https://doi.org/10.1029/2018GL079474>, 2018.

884 Nicholls, Z., Meinshausen, M., Lewis, J., Corradi, M. R., Dorheim, K., Gasser, T., Gieseke,
885 R., Hope, A. P., Leach, N. J., McBride, L. A., Quilcaille, Y., Rogelj, J., Salawitch, R. J.,
886 Samset, B. H., Sandstad, M., Shiklomanov, A., Skeie, R. B., Smith, C. J., Smith, S. J., Su, X.,
887 Tsutsui, J., Vega-Westhoff, B., and Woodard, D. L.: Reduced Complexity Model
888 Intercomparison Project Phase 2: Synthesizing Earth System Knowledge for Probabilistic
889 Climate Projections, *Earth's Future*, 9, e2020EF001900,
890 <https://doi.org/10.1029/2020EF001900>, 2021.

891 Nicholls, Z. R. J., Meinshausen, M., Lewis, J., Gieseke, R., Dommenges, D., Dorheim, K.,
892 Fan, C. S., Fuglestedt, J. S., Gasser, T., Golüke, U., Goodwin, P., Hartin, C., Hope, A. P.,
893 Kriegl, E., Leach, N. J., Marchegiani, D., McBride, L. A., Quilcaille, Y., Rogelj, J., Salawitch,
894 R. J., Samset, B. H., Sandstad, M., Shiklomanov, A. N., Skeie, R. B., Smith, C. J., Smith, S.,
895 Tanaka, K., Tsutsui, J., and Xie, Z.: Reduced Complexity Model Intercomparison Project

896 Phase 1: introduction and evaluation of global-mean temperature response, *Geosci. Model*
897 *Dev.*, 13, 5175-5190, 10.5194/gmd-13-5175-2020, 2020.

898 Norris, J., Hall, A., Thackeray, C. W., Chen, D., and Madakumbura, G. D.: Evaluating
899 Hydrologic Sensitivity in CMIP6 Models: Anthropogenic Forcing versus ENSO, *Journal of*
900 *Climate*, 35, 6955-6968, <https://doi.org/10.1175/JCLI-D-21-0842.1>, 2022.

901 Persad, G., Samset, B. H., Wilcox, L. J., Allen, R. J., Bollasina, M. A., Booth, B. B. B.,
902 Bonfils, C., Crocker, T., Joshi, M., Lund, M. T., Marvel, K., Merikanto, J., Nordling, K., Undorf,
903 S., van Vuuren, D. P., Westervelt, D. M., and Zhao, A.: Rapidly evolving aerosol emissions
904 are a dangerous omission from near-term climate risk assessments, *Environmental*
905 *Research: Climate*, 2, 032001, 10.1088/2752-5295/acd6af, 2023.

906 Persad, G. G., and Caldeira, K.: Divergent global-scale temperature effects from identical
907 aerosols emitted in different regions, *Nature Communications*, 9, 3289, 10.1038/s41467-018-
908 05838-6, 2018.

909 Platnick, S., and Twomey, S.: Remote sensing the susceptibility of cloud albedo to changes
910 in drop concentration, *Atmospheric Research*, 34, 85-98, [https://doi.org/10.1016/0169-
911 8095\(94\)90082-5](https://doi.org/10.1016/0169-8095(94)90082-5), 1994.

912 Popp, T., De Leeuw, G., Bingen, C., Brühl, C., Capelle, V., Chedin, A., Clarisse, L., Dubovik,
913 O., Grainger, R., Griesfeller, J., Heckel, A., Kinne, S., Klüser, L., Kosmale, M., Kolmonen, P.,
914 Lelli, L., Litvinov, P., Mei, L., North, P., Pinnock, S., Povey, A., Robert, C., Schulz, M.,
915 Sogacheva, L., Stebel, K., Stein Zweers, D., Thomas, G., Tilstra, L. G., Vandenbussche, S.,
916 Veefkind, P., Vountas, M., and Xue, Y.: Development, Production and Evaluation of Aerosol
917 Climate Data Records from European Satellite Observations (Aerosol_cci), *Remote Sensing*,
918 8, 421, 2016.

919 Recchia, L. G., and Lucarini, V.: Modelling the effect of aerosol and greenhouse gas forcing
920 on the South Asian and East Asian monsoons with an intermediate-complexity climate
921 model, *Earth Syst. Dynam.*, 14, 697-722, 10.5194/esd-14-697-2023, 2023.

922 Riahi, K., Rao, S., Krey, V., Cho, C., Chirkov, V., Fischer, G., Kindermann, G., Nakicenovic,
923 N., and Rafaj, P.: RCP 8.5—A scenario of comparatively high greenhouse gas emissions,
924 *Climatic Change*, 109, 33, 10.1007/s10584-011-0149-y, 2011.

925 Salzmann, M., Weser, H., and Cherian, R.: Robust response of Asian summer monsoon to
926 anthropogenic aerosols in CMIP5 models, *Journal of Geophysical Research: Atmospheres*,
927 119, 11,321-311,337, <https://doi.org/10.1002/2014JD021783>, 2014.

928 Samset, B. H., Myhre, G., Forster, P. M., Hodnebrog, Ø., Andrews, T., Faluvegi, G.,
929 Fläschner, D., Kasoar, M., Kharin, V., Kirkevåg, A., Lamarque, J. F., Olivié, D., Richardson,
930 T., Shindell, D., Shine, K. P., Takemura, T., and Voulgarakis, A.: Fast and slow precipitation
931 responses to individual climate forcings: A PDRMIP multimodel study, *Geophysical Research*
932 *Letters*, 43, 2782-2791, 10.1002/2016GL068064, 2016.

933 Samset, B. H., Myhre, G., Forster, P. M., Hodnebrog, Ø., Andrews, T., Boucher, O., Faluvegi,
934 G., Fläschner, D., Kasoar, M., Kharin, V., Kirkevåg, A., Lamarque, J. F., Olivié, D.,
935 Richardson, T. B., Shindell, D., Takemura, T., and Voulgarakis, A.: Weak hydrological
936 sensitivity to temperature change over land, independent of climate forcing, *npj Climate and*
937 *Atmospheric Science*, 1, 20173, 10.1038/s41612-017-0005-5, 2018a.

938 Samset, B. H., Sand, M., Smith, C. J., Bauer, S. E., Forster, P. M., Fuglestedt, J. S.,
939 Osprey, S., and Schleussner, C. F.: Climate Impacts From a Removal of Anthropogenic
940 Aerosol Emissions, *Geophysical Research Letters*, 45, 1020-1029,
941 doi:10.1002/2017GL076079, 2018b.

942 Samset, B. H., Lund, M. T., Bollasina, M., Myhre, G., and Wilcox, L.: Emerging Asian aerosol
943 patterns, *Nature Geoscience*, 12, 582-584, 10.1038/s41561-019-0424-5, 2019.

944 Song, F., Zhou, T., and Qian, Y.: Responses of East Asian summer monsoon to natural and
945 anthropogenic forcings in the 17 latest CMIP5 models, *Geophysical Research Letters*, 41,
946 596-603, <https://doi.org/10.1002/2013GL058705>, 2014.

947 Sperber, K. R., Annamalai, H., Kang, I. S., Kitoh, A., Moise, A., Turner, A., Wang, B., and
948 Zhou, T.: The Asian summer monsoon: an intercomparison of CMIP5 vs. CMIP3 simulations
949 of the late 20th century, *Climate Dynamics*, 41, 2711-2744, 10.1007/s00382-012-1607-6,
950 2013.

951 Tebaldi, C., Debeire, K., Eyring, V., Fischer, E., Fyfe, J., Friedlingstein, P., Knutti, R., Lowe,
952 J., O'Neill, B., Sanderson, B., van Vuuren, D., Riahi, K., Meinshausen, M., Nicholls, Z.,
953 Tokarska, K. B., Hurtt, G., Kriegler, E., Lamarque, J. F., Meehl, G., Moss, R., Bauer, S. E.,
954 Boucher, O., Brovkin, V., Byun, Y. H., Dix, M., Gualdi, S., Guo, H., John, J. G., Kharin, S.,
955 Kim, Y., Koshiro, T., Ma, L., Olivie, D., Panickal, S., Qiao, F., Rong, X., Rosenbloom, N.,
956 Schupfner, M., Séférian, R., Sellar, A., Semmler, T., Shi, X., Song, Z., Steger, C., Stouffer,
957 R., Swart, N., Tachiiri, K., Tang, Q., Tatebe, H., Voltaire, A., Volodin, E., Wyser, K., Xin, X.,
958 Yang, S., Yu, Y., and Ziehn, T.: Climate model projections from the Scenario Model
959 Intercomparison Project (ScenarioMIP) of CMIP6, *Earth Syst. Dynam.*, 12, 253-293,
960 10.5194/esd-12-253-2021, 2021.

961 Tian, F., Dong, B., Robson, J., and Sutton, R.: Forced decadal changes in the East Asian
962 summer monsoon: the roles of greenhouse gases and anthropogenic aerosols, *Climate
963 Dynamics*, 51, 3699-3715, 10.1007/s00382-018-4105-7, 2018.

964 Wang, Z., Lin, L., Xu, Y., Che, H., Zhang, X., Zhang, H., Dong, W., Wang, C., Gui, K., and
965 Xie, B.: Incorrect Asian aerosols affecting the attribution and projection of regional climate
966 change in CMIP6 models, *npj Climate and Atmospheric Science*, 4, 2, 10.1038/s41612-020-
967 00159-2, 2021.

968 Webb, D. J.: An ocean model code for array processor computers, *Computers &
969 Geosciences*, 22, 569-578, [https://doi.org/10.1016/0098-3004\(95\)00133-6](https://doi.org/10.1016/0098-3004(95)00133-6), 1996.

970 Westervelt, D. M., Conley, A. J., Fiore, A. M., Lamarque, J. F., Shindell, D. T., Previdi, M.,
971 Mascioli, N. R., Faluvegi, G., Correa, G., and Horowitz, L. W.: Connecting regional aerosol
972 emissions reductions to local and remote precipitation responses, *Atmos. Chem. Phys.*, 18,
973 12461-12475, 10.5194/acp-18-12461-2018, 2018.

974 Wilcox, L. J., Dunstone, N., Lewinschal, A., Bollasina, M., Ekman, A. M. L., and Highwood, E.
975 J.: Mechanisms for a remote response to Asian anthropogenic aerosol in boreal winter,
976 *Atmos. Chem. Phys.*, 19, 9081-9095, 10.5194/acp-19-9081-2019, 2019.

977 Wilcox, L. J., Liu, Z., Samset, B. H., Hawkins, E., Lund, M. T., Nordling, K., Undorf, S.,
978 Bollasina, M., Ekman, A. M. L., Krishnan, S., Merikanto, J., and Turner, A. G.: Accelerated
979 increases in global and Asian summer monsoon precipitation from future aerosol reductions,
980 *Atmos. Chem. Phys. Discuss.*, 2020, 1-30, 10.5194/acp-2019-1188, 2020.

981 Williams, A. I. L., Stier, P., Dagan, G., and Watson-Parris, D.: Strong control of effective
982 radiative forcing by the spatial pattern of absorbing aerosol, *Nature Climate Change*, 12, 735-
983 742, 10.1038/s41558-022-01415-4, 2022.

984 Xian, P., Reid, J. S., Ades, M., Benedettie, A., Colarco, P. R., da Silva, A., Eck, T. F.,
985 Flemming, J., Hyer, E. J., Kipling, Z., Rémy, S., Sekiyama, T. T., Tanaka, T., Yumimoto, K.,
986 and Zhang, J.: Intercomparison of Aerosol Optical Depths from four reanalyses and their
987 multi-reanalysis-consensus, *EGUsphere*, 2023, 1-35, 10.5194/egusphere-2023-2354, 2023.

988 Xie, X., Myhre, G., Liu, X., Li, X., Shi, Z., Wang, H., Kirkevåg, A., Lamarque, J. F., Shindell,
989 D., Takemura, T., and Liu, Y.: Distinct responses of Asian summer monsoon to black carbon
990 aerosols and greenhouse gases, *Atmos. Chem. Phys.*, 20, 11823-11839, 10.5194/acp-20-
991 11823-2020, 2020.

992 Xie, X., Myhre, G., Shindell, D., Faluvegi, G., Takemura, T., Voulgarakis, A., Shi, Z., Li, X.,
993 Xie, X., Liu, H., Liu, X., and Liu, Y.: Anthropogenic sulfate aerosol pollution in South and East
994 Asia induces increased summer precipitation over arid Central Asia, *Communications Earth
995 & Environment*, 3, 328, 10.1038/s43247-022-00660-x, 2022.

996 Zelinka, M. D., Andrews, T., Forster, P. M., and Taylor, K. E.: Quantifying components of
997 aerosol-cloud-radiation interactions in climate models, *Journal of Geophysical Research:
998 Atmospheres*, 119, 7599-7615, 10.1002/2014JD021710, 2014.

999 Zelinka, M. D., Smith, C. J., Qin, Y., and Taylor, K. E.: Comparison of methods to estimate
1000 aerosol effective radiative forcings in climate models, *Atmos. Chem. Phys.*, 23, 8879-8898,
1001 10.5194/acp-23-8879-2023, 2023.

1002 Zhang, X. Y., Wang, Y. Q., Niu, T., Zhang, X. C., Gong, S. L., Zhang, Y. M., and Sun, J. Y.:
1003 Atmospheric aerosol compositions in China: spatial/temporal variability, chemical signature,
1004 regional haze distribution and comparisons with global aerosols, *Atmos. Chem. Phys.*, 12,
1005 779-799, 10.5194/acp-12-779-2012, 2012.

1006